REVIEW

Non-isothermal grain growth in metals and alloys

S. Mishra and T. DebRoy*

A large portion of the previous research on grain growth has been focused on isothermal conditions and excellent reviews on this topic are available in the literature. However, most of the materials processing operations such as casting, rolling and welding take place under non-isothermal conditions. Grain growth in materials under significant spatial and temporal variation of temperature exhibits many important special characteristics. The present paper critically examines these special features of grain growth in several important materials processing operations. Various experimental and theoretical approaches used to study grain growth in non-isothermal systems are examined and compared. The classical isothermal grain growth theories are reviewed, because they are sometimes applied to non-isothermal systems by incorporating thermal history in the calculations. Various numerical techniques and their applications to non-isothermal systems are also examined and compared. Finally, progress made in understanding non-isothermal grain growth in metals and alloys is summarised and several areas of future research are identified. This review is targeted towards an audience of materials scientists and engineers interested in various materials processing operations under non-isothermal conditions.

Keywords: Grain growth, Welding, Casting, Rolling, Annealing, Monte Carlo, Cellular automaton, Phase field

Introduction

Grain growth in isothermal systems has been studied extensively,[1–44] and excellent reviews are available in the literature on this topic.[1–5] However, most of the materials processing operations involve heating and cooling, and the material experiences spatial and/or temporal variations of temperature during processing. Although the effect of temperature on grain growth has been extensively studied in isothermal systems, such studies do not reveal many unique features of grain growth observed in real materials processing systems. So far, no comprehensive single review is available to beginner researchers who are interested in grain growth during materials processing such as welding, cyclic annealing, casting and hot rolling.

The special features of the non-isothermal materials processing systems can be appreciated by considering a few examples. Cyclic annealing involves rapid ramping up and down of temperature at different rates, with isothermal holds at the maximum and the minimum temperatures. This treatment significantly accelerates growth of ferrite grains in steel specimens. What is special here is that the grain size is much larger than that obtained for isothermal treatment at the maximum temperature.[45] What is the effect of frequency and amplitude of temperature cycles, and isothermal holding times at high and low temperatures on grain growth kinetics? The answer to this question is important for cyclic annealing and it also reflects on the current state of understanding of grain growth. Fusion welding is characterised by transfer of heat within the workpiece by conduction and convection, often in a short time frame.[46,47] During welding, the heat affected zone (HAZ) experiences steep spatial temperature gradients that change with time. It is well known that higher temperatures favour grain growth. What is important and less well known is that the steep temperature gradients tend to retard grain growth. These two opposite effects interact during grain growth in the HAZ. Results of isothermal studies cannot directly explain, in a quantitative manner, the complex effects of spatial and temporal variations of temperature. Casting of metals involves continuous cooling cycles. Unlike slow, controlled cooling, where the grain structure is allowed to attain equilibrium at each cooling step, continuous cooling causes significant spatial temperature gradients, which prevent formation of uniform grain structure. Often a spatial variation of grain structure is observed where columnar grains are formed first, and later the columnar grain growth is restricted by the equiaxed grains that form in front of the columnar grains. How is the columnar to equiaxed transition (CET) affected by temperature variation in the casting? Is there a quantitative link between the temperature gradients and the rate of grain growth?[48] The answers to these questions are important for better understanding of the mechanism of grain growth during casting.

Department of Materials Science and Engineering, The Pennsylvania State University, University Park, PA 16802, USA

*Corresponding author, email debroy@psu.edu

Published by Maney on behalf of the Institute
Received 9 August 2005; accepted 31 October 2005
DOI 10.1179/174328406X84094

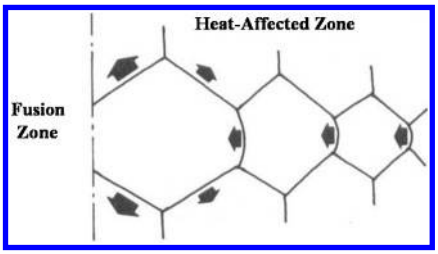

1 Rapid change in grain size, under steep temperature gradient in HAZ, may lead to changes in shapes of grains, which in turn may hinder grain growth: arrows in figure indicate direction of motion of respective grain boundaries[51]

During hot rolling and casting, addition of inoculants is a common practice to achieve refined grain size.[48] The inoculants are very effective in 'pinning' grain growth. The effectiveness of the inoculants depends on temperature, because the inoculants may dissolve in the alloy above a certain temperature. Thus, it is important to understand how the variation of temperature during hot rolling and casting affects dissolution of inoculants and grain growth.

In this review, various experimental and theoretical approaches used to study grain growth in non-isothermal systems are critically examined. The experimental techniques for determining grain size include measurements on post processed specimens as well as *in situ* real time measurements. A brief discussion of the analytical studies of grain growth in isothermal systems is included to examine their adaptation to non-isothermal systems. Numerical techniques for the simulation of non-isothermal grain growth such as cellular automaton (CA) method, Monte Carlo (MC) technique and phase field (PF) approach are discussed and their applications are examined. Recent advancements in the field and the special features of grain growth under non-isothermal conditions, which cannot be understood by isothermal studies, are highlighted. These special features include enhanced grain growth in cyclic annealing as compared with isothermal heating at the maximum temperature of the cycle, 'thermal pinning' observed in the HAZ of welds where steep temperature gradients inhibit grain growth, CET in castings and the dissolution of grain growth inhibiting inoculants at high temperatures during hot rolling and casting. The applications of various numerical techniques in understanding non-isothermal grain growth during materials processing are examined. Finally, the progress made is summarised and several areas of future research are identified.

Special features of non-isothermal grain growth

Heat affected zone of welds

Weld HAZ experience significant spatial and temporal temperature variations. Locations close to the fusion plane experience strong thermal cycles with peak temperatures close to the solidus temperature, while locations further away experience less intense thermal cycles. Furthermore, steep temperature gradients exist in the HAZ close to the fusion plane. Alberry *et al.*[49,50] found that the steep temperature gradients in the HAZ

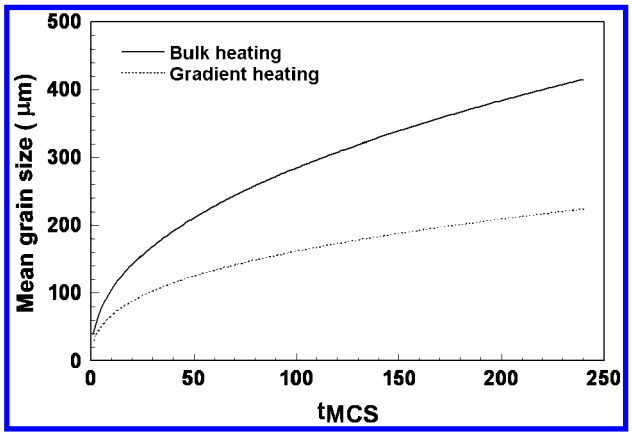

2 Kinetics of grain growth at distance of 1 mm from fusion plane on midsection vertical symmetry plane in HAZ of Ti–6Al–4V alloy weld fabricated with heat input of 2·13 MJ m^{-1}: dotted curve represents kinetics under steep temperature gradients in HAZ (gradient heating); solid line represents kinetics when bulk material is subjected to uniform thermal cycle observed at 1 mm from fusion plane on midsection vertical symmetry plane (bulk heating); rate of growth is much faster in latter case; two curves were calculated using 3D MC model for grain growth[52]

inhibit grain growth owing to the 'thermal pinning' effect, which is explained as follows. The steep temperature gradients cause the atomic mobility to vary across a large grain causing different parts of the grain to have different propensities to grow. The growth of any individual grain under a temperature gradient is restrained by the more rapid growth of neighbouring grains at higher temperature regions. Another possible explanation[51] for 'thermal pinning' is that grains that have a large temperature gradient across them tend to grow non-uniformly, resulting in a change of shape from, say, equiaxed to pear shaped, as shown in Fig. 1. The corresponding increase in surface to volume ratio effectively represents an increase in energy, thereby neutralising the reduction in energy present in normal grain growth.

The 'thermal pinning' effect is best demonstrated from the computed results of three-dimensional (3D) MC grain growth model. Figure 2 compares the grain growth kinetics under steep temperature gradients in a weld HAZ with the grain growth kinetics resulting from the same thermal cycle but in the absence of temperature gradients, i.e. 'bulk heating'. During bulk heating, an entire domain is subjected to the same thermal cycle so that no spatial gradient of temperature exists in the specimen.[52] The dotted curve shows the computed grain growth kinetics in the HAZ of a Ti–6Al–4V weld at a monitoring location 1 mm away from the fusion plane on the midsection vertical symmetry plane. This curve represents the grain growth kinetics under steep spatial temperature gradients. The solid line in Fig. 2 shows the computed grain growth kinetics at the same location under 'bulk heating' where the entire calculation domain was subjected to the same thermal cycle as the monitoring location in the weld HAZ. It is observed that the growth rate is much faster during 'bulk heating' indicating retardation of grain growth owing to thermal pinning in the HAZ.

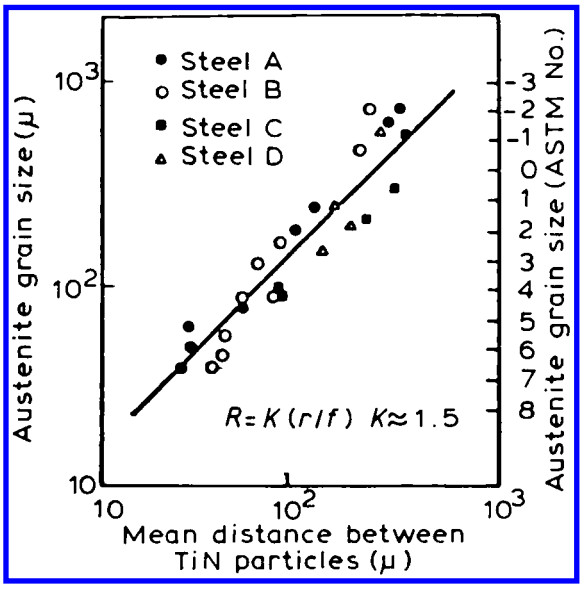

3 Austenite grain size *R* versus mean distance between TiN precipitates in four steels: smaller mean distance between TiN precipitates, more effective is pinning of austenite grain growth; expression shown in figure relates austenite grain size *R* with precipitate size *r* and volume fraction of precipitates *f*, where *K* is dimensionless constant[54]

Precipitate pinning is another factor that significantly affects the grain size in the HAZ. For example, TiN, which is one of the most stable precipitates in steel, is often used to control austenite grain size in steel welds. It has been shown that steels with a dispersion of TiN precipitates of appropriate size and volume fraction, can hinder grain growth up to temperatures of about 1200–1250°C.[51,53] Figure 3 shows the experimental results of Matsuda and Okumura,[54] where they illustrated the relation between grain size, precipitate size and volume fraction for four different kinds of steel. Figure 3 clearly shows the strong influence of TiN precipitates on the austenite grain size in steels.

An important feature of the HAZ grain structure is the occurrence of large grain size close to the fusion plane owing to stronger thermal cycles.[49,52] Thus, the grain size in the HAZ is affected by both the temperature gradient and the thermal cycles. The effects of these two important factors have been isolated in a recent study[55] and the effects of these two variables will be discussed more completely in a subsequent section of the present paper.

Cyclic annealing

Cyclic annealing involves rapid ramping up and down of temperature at different rates, with intermediate holds at the maximum and the minimum temperatures.[45,56–61] This treatment has been found to significantly accelerate grain growth of ferrite in steel specimens.[45] What causes this enhanced growth? What effects do intermediate holds, cycle frequency and thermal amplitude have on grain growth kinetics? Sahay *et al.*[45] addressed these issues in a recent study on aluminium killed (AlK) steel (0·05 wt-%C, 0·05 wt-%Al and 45 ppm N). A typical heat treatment schedule during cyclic annealing is illustrated in Fig. 4*a*. It consists of five components:

(i) an upper limiting temperature T_{high}, kept constant at 725°C

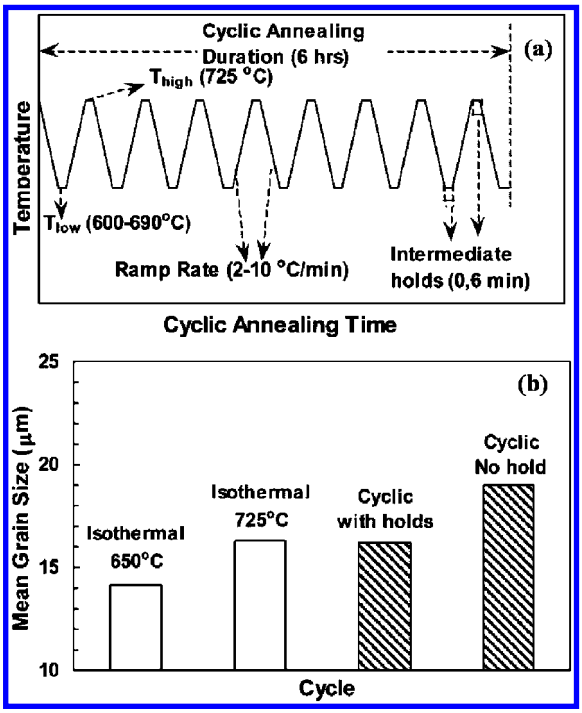

4 *a* schematic representation of thermal cycles during cyclic annealing[45] and *b* comparison of mean grain size in isothermally annealed specimens with that in cyclically annealed specimens[45]

(ii) a lower limiting temperature T_{low}, varied between 600 and 690°C in different experiments

(iii) heating and cooling rates (ramp rate) between T_{low} and T_{high} varied between 2 and 10 K min^{-1}

(iv) isothermal intermediate holds at T_{low} and T_{high}, either for 0 or 6 min

(v) total duration of cyclic annealing, kept constant at 6 h.

In comparing the mean grain size for cyclic annealing with that for isothermal annealing, as shown in Fig. 4*b*, Sahay *et al.*[45] found that the mean grain size of the cyclically annealed specimen over a total time of 6 h was 16·5% larger than the mean grain size of the specimen isothermally annealed at 725°C, i.e. the upper limiting temperature of the cycle, for 6 h. This result is unexpected because during cyclic annealing, the specimen was subjected to temperatures that were lower than the upper limiting temperature for a portion of the total six hour duration. Sahay *et al.*[45] suggested that during cyclic annealing, in addition to thermal excitation in isothermal grain growth, an 'extra excitation' is available. The extra excitation increases the grain boundary mobility and reduces the effective activation energy for grain growth, thus resulting in accelerated grain growth.

Sahay *et al.*[45] also studied the effects of isothermal intermediate holds at T_{low} and T_{high}, cycle frequency and temperature amplitude on grain growth kinetics. They[45] observed an unexpected decrease in mean grain size when isothermal intermediate holds were introduced in the cycles. Grain size increased with cycle frequency when T_{high} and T_{low} were kept constant. Furthermore, grain size increased with decrease in T_{low}. These observations cannot be explained on the basis of isothermal grain growth kinetics, which do not capture non-isothermal effects such as heating rate and

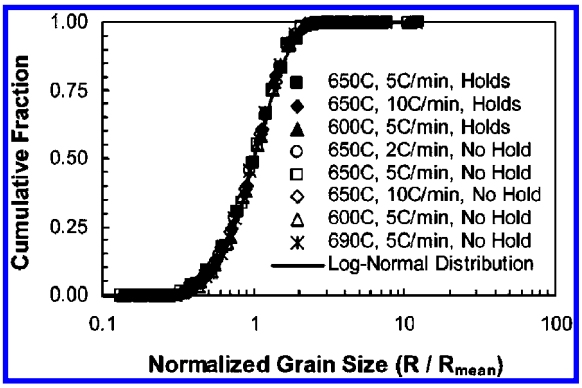

5 Invariant nature of normalised grain size distributions[45]

temperature reversal effects imposed during cyclic annealing. Furthermore, the concept of 'extra excitation' used by Sahay *et al.*[45] to explain the grain growth in cyclic annealing, remains to be quantitatively understood from the consideration of physical processes.

Shuh and Dunand[56] studied uniaxial hot pressing of zinc powders during cyclic annealing. They found that the rate of densification during cyclic annealing was higher than that during isothermal densification at the upper cycle temperature. In another study, Geng *et al.*[57] observed an acceleration of age hardening kinetics in Ti–6Al–4V alloy during cyclic age hardening treatments between 77 and 623 K. Although there are inherent similarities in these observations, a unified mechanism of grain growth during cyclic annealing remains to be developed.

Sahay *et al.*[45] also studied normalised grain size distributions in specimens subjected to different cyclic annealing conditions, as shown in Fig. 5. They[45] found that although the specimens were heat treated with widely different cycle parameters, their normalised grain size distributions were invariant. This result is consistent with that observed in the HAZ of welds, where the normalised grain size distributions for different thermal cycles were found to be the same.[52] Mishra and DebRoy[52] related these results to the time invariance of grain size distributions during normal grain growth observed in different materials.[10,12,15] They argued that such a behaviour could be explained by considering any thermal cycle in the HAZ as a collection of a large number of discrete isothermal steps applied for different times. Therefore, the grain size distribution under different thermal cycles behaved in a similar manner as that under different isothermal conditions for different times, i.e. remained invariant. Furthermore, as shown by the solid line in Fig. 5, the normalised grain size distributions followed a lognormal distribution.

Casting

Casting of metallic alloys may exhibit either wholly columnar or entirely equiaxed grain structures, depending on the alloy composition and the solidification conditions. A more complex structure, composed of both types of grains, is often observed in chill castings. This mixed mode of solidification occurs if equiaxed grains can grow in the bulk liquid ahead of the advancing columnar front, resulting in a transition from a columnar zone to an equiaxed zone in some as cast structures.[62] Figure 6*a* shows the experimentally determined grain structure in a longitudinal section of an Al–7Si (wt-%) ingot.[63] Figure 6*b* shows the corresponding computed grain structure.[63] Among many grains formed at the bottom surface of the ingot only a few long columnar grains succeed in growing. At about midheight of the casting, the undercooled liquid region ahead of the columnar dendrite tips becomes wider because of

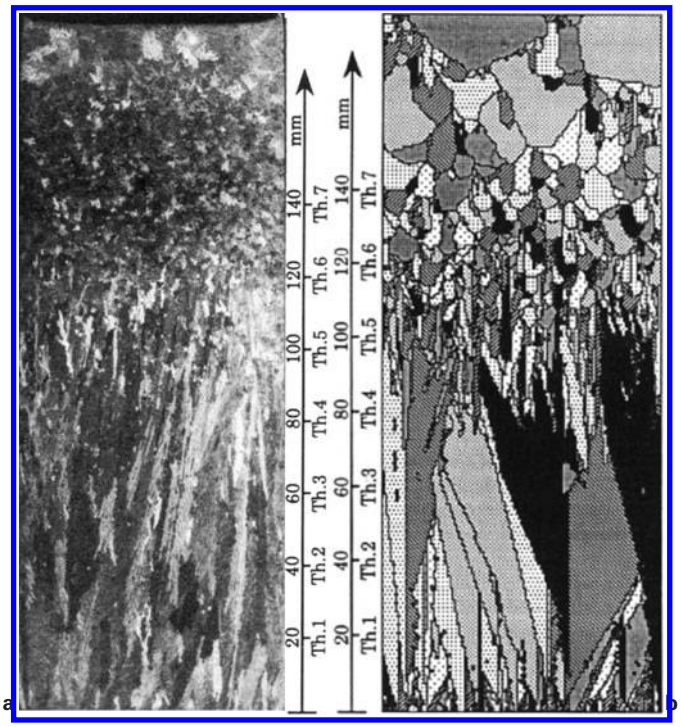

6 *a* grain structure in longitudinal section of Al–7Si alloy cylinder unidirectionally solidified over copper chill plate[63] and *b* grain structure calculated with CA–finite element (FE) model for longitudinal section of Al–7Si ingot shown in part *a*[63]

lower temperature gradient. Grains nucleate in the bulk of the liquid, grow and finally stop the columnar front. However, these grains still have an elongated shape because of the temperature gradient. As the temperature gradient continues to decrease in the remaining liquid, such grains finally become truly equiaxed in the upper part of the casting. In Fig. 6, the presence of a few larger equiaxed grains could be observed near the top surface of the ingot. Thus, the long columnar grains become more equiaxed as the temperature gradient decreases. The grain structure in Fig. 6 indicates the strong effect of the temperature variation on grain growth in castings.

The prediction of the CET and the relative volume of the columnar and equiaxed zones[64] are of interest, because they affect the mechanical properties of solidified products. For small specimens of almost uniform temperature, experimental observations indicate that the growth of the equiaxed grains ahead of the columnar front is the most important mechanism for causing the CET.[65] For large castings, the temperature field significantly affects the competitive columnar and equiaxed solidification, because columnar growth is constrained by the movement of the isotherms, and equiaxed growth ahead of the columnar front alters the temperature field through the release of the latent heat. A detailed investigation of the mechanism of grain growth is needed to develop a better understanding of the CET phenomenon in castings.

Hot rolling

During hot rolling of plain carbon steel, the austenite grain size affects the final ferrite morphology and the resulting mechanical properties, i.e. the strength and toughness of the steel.[66] How do the thermal conditions during hot rolling affect the austenite grain size? Does the preheating schedule have any impact on the austenite growth kinetics? In order to address these questions, Militzer *et al.*[66] investigated austenite grain growth kinetics in A36 steel (0·17C–0·74Mn, wt-%) under thermal conditions similar to those during hot rolling. They[66] compared austenite grain growth in two specimens, which were heated at different rates, i.e. 5 and 100 K s^{-1}, from room temperature to 1100°C, and then held at this temperature for a fixed duration. They[66] found that a slower heating rate resulted in larger average grain size. Figure 7 shows that the equivalent area diameter (EQAD) was 140 μm in the specimen

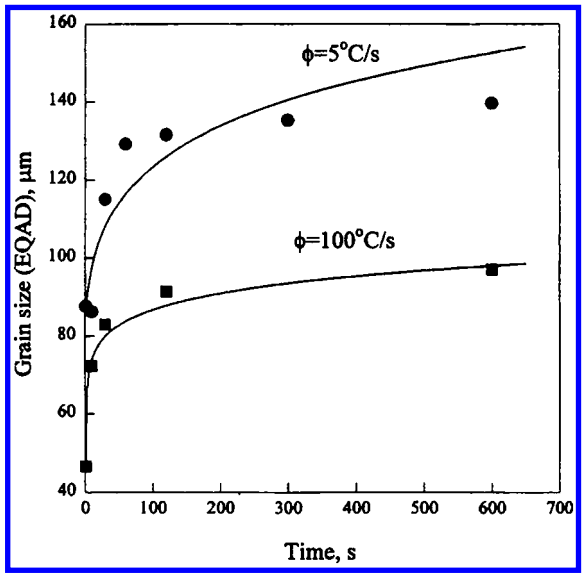

7 Comparison of austenite grain growth at 1100°C in A36 steel after heating at different rates ϕ; experimental results and lines representing fit to empirical power law for grain growth are shown[66]

subjected to an initial heating rate of 5 K s^{-1} and 100 μm in the specimen heated at 100 K s^{-1}. The grain growth rates depended strongly on the preheat schedule, because the preheat determined the size and volume fraction of AlN precipitates in A36 steel. These precipitates form an integral part of A36 steel at temperatures <1150°C and cause 'pinning' of grain growth. Thus, the final austenite grain size in A36 steel is strongly influenced by preheat schedule. Leap and Brown[67] found that in high nitrogen steels containing niobium and aluminium, AlN and Nb(C,N) precipitates have good thermodynamic stability over the range of austenitising temperatures, and hence provide significant resistance to grain growth.

Comparison of special features of grain growth in various materials processing

Table 1 compares the special features of non-iothermal grain growth in the HAZ of welds, and in specimens from cyclic annealing, casting and hot rolling. Table 1 also compares the special non-isothermal conditions observed during these materials processes. The weld HAZ experiences steep temperature gradients and

Table 1 Special features of grain growth in various non-isothermal processes

	Hot rolling	Casting	Cyclic annealing	Welding (HAZ)
Temperature change	Slow and rapid change of temperature with time	Slow temperature change	Rapid heating and cooling with isothermal holds at the two extreme temperatures	Steep spatial gradient of temperature and strong thermal cycles
Special features	Slow heating rates lead to large grains	Entirely columnar or entirely equiaxed or mixed grain structure	Grain size distribution is unaffected by process conditions	Significant spatial gradient of grain size
		Columnar to equiaxed transition (CET) is facilitated by low pouring temperature and small temperature gradient	Enhanced grain growth as compared with isothermal annealing	Grain size distributions and topological class distributions are spatially invariant. 'Thermal pinning' of growth owing to steep temperature gradients
			Increase in grain size with increasing cycle frequency	

strong thermal cycles close to the fusion plane, while cyclic annealing involves rapid heating and cooling with isothermal intermediate holds at the maximum and the minimum temperatures of the cycle. Casting and hot rolling experience relatively slower temperature changes with time. The steep temperature gradients in the HAZ cause the thermal pinning of grain growth, while the spatial variation of thermal cycles causes significant spatial variation of grain size. The cyclic annealing causes enhanced growth as compared with isothermal annealing and the grain size increases with cycle frequency. The grain structure in castings is often a mixture of both elongated and equiaxed grains, and the CET is very important for the mechanical properties of castings. Hot rolling leads to relatively large grains, which are generally refined by adding inoculants to the material. In both cyclic annealing and the weld HAZ the normalised grain size distribution is unaffected by the thermal cycles.

Techniques for experimental determination of grain structure

Grain structure measurements on processed specimens

Table 2 presents a comparison of different experimental methods used for the characterisation of grain structure. Average grain size, perhaps the most important parameter in characterising grain structure, is commonly measured by the lineal intercept method on post processed specimens. The grain structure is revealed on a surface of interest after careful grinding, polishing and etching operations, using an optical microscope, as described in many text books. In order to determine the average grain size, random straight lines are drawn on a micrograph and the numbers of grains that intersect each line are counted. The average grain size along each line is calculated by dividing the length of the line by the number of grain intersections. The average of the measurements along all the lines gives the average grain size for the specimen. Table 2 indicates that the lineal intercept method measures the average grain size on two-dimensional (2D) cross-sections. This value is smaller than the actual average grain size in 3D, because most arbitrarily selected lines do not pass through the centre of the grain. When the goal is to obtain the 3D grain size in a specimen, serial sectioning technique is used. As indicated in Table 2, serial sectioning involves cutting a specimen layer by layer, and characterising grain structure of each layer. Thus, serial sectioning is a very tedious and time consuming process and is successful only when the grain size is not very small. Other features of the grain structure that are important include grain size distribution and grain topology. Grain size distribution is obtained by measuring the actual size of each grain in the specimen. Counting the number of edges of each grain provides an important feature of grain topology. Image recognition software can track the grain boundaries and make the measurements simpler and faster. However, software assisted measurements require that the grain boundaries are clearly revealed by metallography with good contrasts. Because it is a difficult task to clearly reveal grain boundaries in many materials, the image recognition software must be used with caution and computer assisted measurements should be checked manually in some specimens to ensure their reliability.

The methods mentioned so far involve measurements on post processed specimens. They do not give any information about the evolution of grain structure during processing. The conventional approach to capture real time effects involves quenching large number of specimens after different durations of processing and then measuring grain size or characterising grain structure on each specimen. However, this technique is time consuming and expensive, and the time resolution is

Table 2 Experimental techniques for measurement of non-isothermal grain growth

	Lineal intercept method	Serial sectioning	Laser ultrasonics
Principle	Random straight lines are drawn on a micrograph; average grain size along each line is equal to the length of the line divided by the number of grain intersections; the average of the measurements along all the lines gives the average grain size for the specimen	Successive cross-sections are cut in a 3D specimen to reveal the grain structure	Reduction in intensity of the ultrasonic waves owing to scattering by austenite grains gives grain size
Average grain size	Yes (2D)	Yes	Yes
Actual grain size (3D)	No	Yes	No
Topology	Yes	Yes	No
Real time	Poor time resolution	Poor time resolution	Yes
Specific advantages	Ordinary light microscope can be used. Gives average grain size from micrometre to centimetre scale	Gives 3D grain size from micrometre to centimetre scale	Very small time resolution. A remote technique with standoff distances of 1 m. Works well at high temperatures. Tracks average grain size at various temperatures during an experiment. Requires little or no specimen preparation
Limitations	Requires careful specimen preparation and specific etchants. Time consuming	Very tedious and time consuming	Cannot measure size <100 μm
Application	Post processed specimens	Post processed specimens	Hot rolling, HAZ of welds

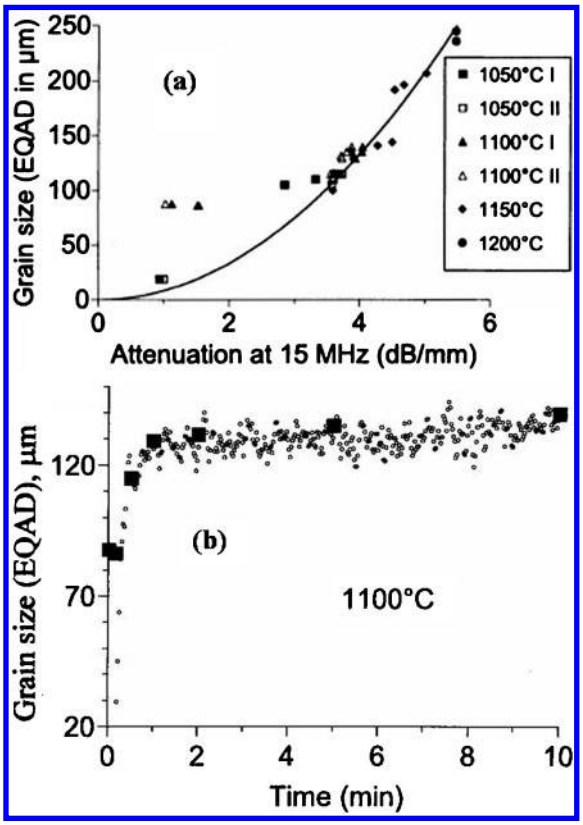

8 ***a*** **austenite EQADs in A36 steel measured by metallography versus 15 MHz ultrasonic attenuation at 1100°C: solid line is parabolic least square fit and** ***b*** **comparison of austenite EQADs estimated from ultrasonic attenuation measurements (○) with those measured by metallography (■) for austenitisation at 1100°C in A36 steel specimens; time** $t=0$ **corresponds to time at which temperature measured by thermocouple spot welded on specimen reached austenitising temperature[69]**

generally poor. The laser ultrasonic[68–70] technique allows *in situ* measurement of average grain size and is characterised by very good time resolution, remote access and high temperature measurement capability. It also does not require any elaborate specimen preparation.

Real time measurements

Laser ultrasonics[68,69] has been recently developed to measure real time grain growth kinetics quantitatively in steels during hot rolling. Laser ultrasonics is based on the generation of ultrasonic waves by a pulsed laser and the subsequent detection of these waves by a laser interferometer.[71] It is a remote technique[71] with standoff distances of the order of 1 m, and works well at high temperatures for steels.[72] It is based on the principle that for most hot rolled carbon steels, ultrasonic attenuation, i.e. the reduction in intensity of the ultrasonic waves is primarily caused by the scattering of waves by the bulk of the grain. Thus, in the case of austenite grain growth, ultrasonic attenuation increases with increasing grain size.[68]

The time resolution of this procedure is good and it does not require any lengthy procedure involving polishing, etching, metallography and grain structure analysis on post-processed specimens. This procedure requires little or no specimen preparation. Dubois *et al.*[69]

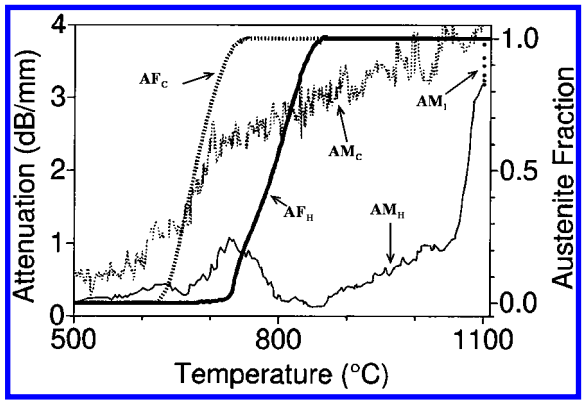

9 Attenuation measurements in A36 steel specimen during heating (thin solid line marked by AM_H**), cooling (thin dotted line marked by** AM_C**) and isothermal treatment at 1100°C (bold dots marked by** AM_I**): austenite fractions measured by dilatometry during heating (thick solid line marked by** AF_H**) and cooling (thick dotted line marked by** AF_C**), are also indicated[68]**

showed that this procedure can be used for quantitative measurement of grain size in A36 steel. In order to quantitatively relate ultrasonic attenuation to austenite grain size, a calibration was obtained based on the metallographic evaluation of the austenite grain size on quenched specimens of A36 steel, as shown in Fig. 8*a*. The EQAD, i.e. the diameter of a circle with an area equal to the mean area of the measured grains, was chosen to quantify grain size. The solid line in Fig. 8*a* is a parabolic fit of the EQADs >100 μm to the 15 MHz ultrasonic attenuation at 1100°C. The ultrasonic attenuation was calibrated in terms of EQAD for austenite grains >100 μm as[69]

$$D = C\alpha_{1100}^2 \quad (1)$$

where D is the austenite grain size (EQAD in μm), $C=8{\cdot}31$ μm (mm^2 dB^{-2}) and α_{1100} is the 15 MHz ultrasonic attenuation at 1100°C. Furthermore, Dubois *et al.*[69] noted that for grain size <100 μm, the number of data points was insufficient to validate the calibration. Using equation (1), laser ultrasonic attenuation values were converted to grain size and plotted as a function of time for different austenitising temperatures. The plot for an austenitising temperature of 1100°C is shown in Fig. 8*b*. The metallographic measurements by the linear intercept method are included as solid squares. Good agreement was observed between the measurements using the laser ultrasonics and the linear intercept methods. The rapid increase in grain size in the first minute and the subsequent slow changes indicated by the metallographic measurements were correctly reproduced by laser ultrasonic measurements with good time resolution.

In an earlier paper, Dubois *et al.*[68] conducted laser ultrasonic attenuation measurements during a thermal cycle in hot rolled A36 steel at temperatures between 500 and 1100°C. The thermal cycle included heating from room temperature to 1100°C at a rate of 5 K s^{-1}, holding at this temperature for 10 min, and cooling at a rate of 1 K s^{-1}. The ultrasonic attenuation is presented as a function of temperature in Fig. 9. The austenite fractions determined by dilatometry are also shown in Fig. 9 for comparison with the phase transformation

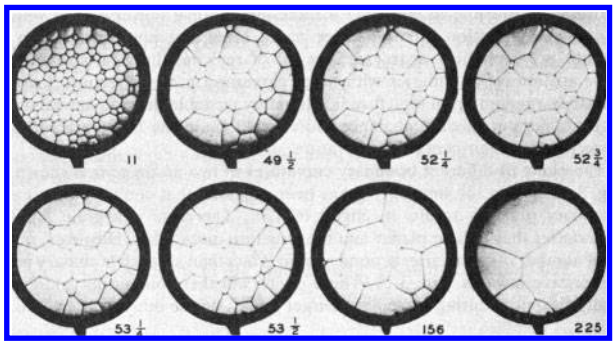

10 Two-dimensional cells of soap froth illustrating process of grain growth: numbers are time in minutes[22]

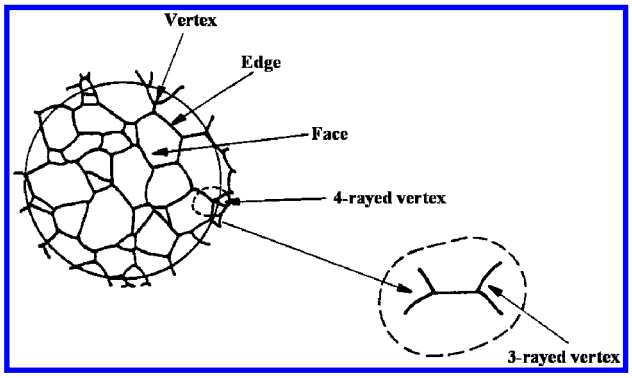

11 Typical 2D section through 3D grain structure: 4-rayed vertex will tend to decompose into two 3-rayed vertices as grain growth occurs[2]

kinetics obtained from ultrasonic attenuation. The variations of ultrasonic attenuation were related to microstructural changes caused by the austenite–ferrite phase transformation and austenite grain growth. During heating of steel to 1100°C, the ultrasonic attenuation dropped between 720 and 900°C owing to ferrite to austenite transformation. During this transformation, austenite nucleates and forms a finer microstructure than the prior ferritic structure. The smaller austenite grains lead to a decrease in the ultrasonic attenuation.[68] The minimum attenuation was observed at ~860°C when the ferrite to austenite transformation completed, as confirmed by the dilatometry measurements. Above 900°C, the attenuation increased slowly till 1050°C, above which a rapid increase in attenuation was observed. Up to 1050°C the growth rate of austenite grains is slow, because of the presence of AlN precipitates in the steel. However, the AlN precipitates dissolve >1050°C leading to rapid austenite grain growth[66,73] and, as a result, a marked increase in ultrasonic attenuation is observed. Once the ultrasonic attenuation is converted to the corresponding austenite grain size based on equation (1), the results[68] can give a quantitative description of austenite grain growth kinetics. This approach was adopted by Kruger *et al.*,[70] who used laser ultrasonics technique to monitor austenite grain growth in A36 steel under thermal cycles similar to those experienced by the HAZ of welds. The thermal cycles were generated by a Gleeble 3500 thermomechanical simulator. The final austenite grain size obtained by the laser ultrasonics technique agreed with the prior austenite grain size measured by metallography within the range of accuracy of the metallographic measurements. Thus, although the laser ultrasonics technique requires specialised equipment, it can provide average grain size evolution data in non-isothermal systems during materials processing.

Another emerging method for real time measurement of grain growth is 3D X-ray diffraction microscopy.[74] This is a non-destructive method for dynamic characterisation of grains within polycrystalline materials.[74,75] The method is based on diffraction with highly penetrating X-rays, enabling 3D studies of several millimetre thick specimens. The position, volume and orientation can be derived for hundreds of grains simultaneously. 3D maps of the grain boundaries can be generated by applying novel reconstruction methods. Poulsen *et al.*[74] demonstrated the capabilities of this method by applying it to study grain growth during annealing of polycrystalline aluminium (Al). 3D maps of grains were generated with a spatial resolution of ~5 μm. More and more applications of this method are appearing in the literature, and although it has not been applied to study grain growth in non-isothermal systems, it holds significant promise for the future.

Analytical solutions for grain growth

As discussed before, grain growth in non-isothermal systems has many special features and most of the earlier studies were focused on understanding normal grain growth phenomenon in isothermal systems.[1–44] A brief discussion of the theories of grain growth in isothermal systems is presented here, because they serve as a basis for understanding grain growth in more complex non-isothermal systems.

Topological constraints

In the early 1950s, Smith[22] proposed that soap froth evolution is an analogue to grain growth. He[22] suggested that normal grain growth results from the interaction between the topological requirements of space filling and the need for surface tension equilibrium. The froth structure, as shown in Fig. 10, resembles a grain structure where the grain boundary energy is isotropic, i.e. independent of grain orientation. Only 2D geometry is considered for simplicity. The grain structure consists of vertices joined by edges (also called 'sides') that envelope the cross-section of a cell in 2D. The coordination number z of a vertex is given by the number of edges joined to it. The requirement of surface tension equilibrium eliminates the vertices at which more than three cells meet.[22] Therefore, the stable coordination number is three for 2D. This means that a 4-rayed vertex will be unstable and will tend to decompose into two 3-rayed vertices as shown in Fig. 11. This also means that an equilibrium 2D structure, with all the boundaries having the same surface tension, has angles of 120° at the vertex and the average number of edges surrounding a cell $\langle n \rangle$ is six (here, a cell refers to a 2D cross-section of a 3D froth cell). The validity of 120° angle can be justified by the following simple arguments. Consider a wire frame suspending a liquid film, as shown in Fig. 12*a*. If one bar of the frame is movable, then a force F per unit length must be applied to maintain the bar in position.[5] If this force moves a small distance so that the total area of the film is increased by dA, the work performed by the force is $F\,dA$. The present work is used to increase the free energy of the system by dG, which is given by the

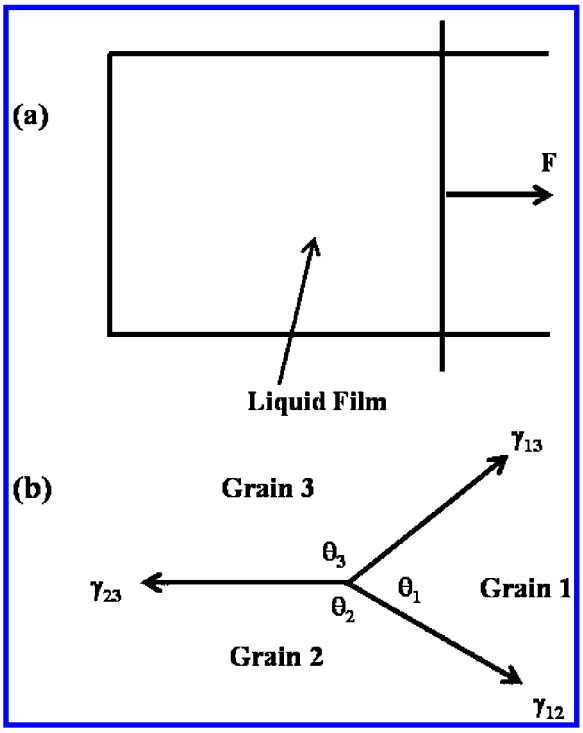

12 ***a*** **liquid film on wire frame and** ***b*** **balance of grain boundary tensions for grain boundary intersection in metastable equilibrium (after Ref. 5)**

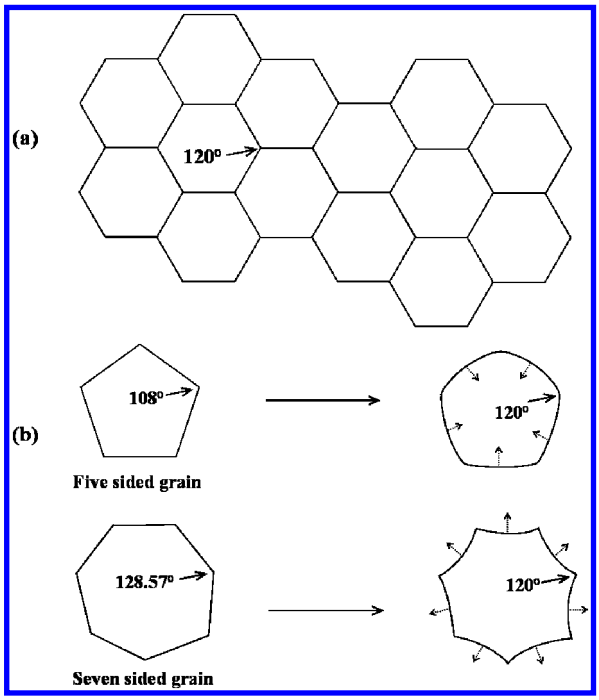

13 ***a*** **two-dimensional grain structure containing all six sided grains: grain structure is in equilibrium when all vertex angles are 120° and** ***b*** **edges of five sided grain become concave inwards and edges of seven sided grain become concave outwards in order to attain 120° vertex angle: curved grain boundaries move towards their centre of curvature to reduce surface area[76]**

following expression[5]

$$dG=\gamma dA+Ad\gamma \tag{2}$$

where γ is the excess free energy of the interface. Equating dG in equation (2) with $F\,dA$ gives

$$F=\gamma+A\,\frac{d\gamma}{dA} \tag{3}$$

in the case of a liquid film, the surface energy is independent of the area of the interface and $d\gamma/dA=0$. This leads to the well known result

$$F=\gamma \tag{4}$$

i.e. a surface with a free energy γ (J m^{-2}) exerts a surface tension of γ (N m^{-1}).

However, in the case of interfaces involving solids, it is not immediately obvious that γ is independent of area. Consider a 2D section of a grain structure where three grains meet at a point, as shown in Fig. 12*b*. If the boundary energy is independent of grain orientation, the grain boundary behaves like a soap film.[5] Under these conditions the metastable equilibrium at a junction between three grains requires that the boundary tensions, γ_1, γ_2 and γ_3 must balance, which means

$$\frac{\gamma_{23}}{\sin\theta_1}=\frac{\gamma_{13}}{\sin\theta_2}=\frac{\gamma_{12}}{\sin\theta_3} \tag{5}$$

now, if all the grain boundaries in a polycrystal are assumed to have the same grain boundary energy, equation (5) predicts that $\theta_1=\theta_2=\theta_3=120^\circ$.

It is important to point out here that the structure described above is at metastable equilibrium. Unlike a single crystal, completely equilibrium structure is not possible in a polycrystal because of the presence of grain boundaries, which are high energy locations.[5] Considering the resemblance between froth and grain structure, Smith[22] argued that unless all the grains in a structure are six sided, grain growth will occur (here 'grain' refers to a 2D cross-section of an actual 3D grain). A six sided grain has all its angles equal to 120°. Therefore, a grain structure with only six sided grains, as shown[76] in Fig. 13*a*, and with all edges having the same energy, will have all vertex angles as 120° and will remain in a metastable equilibrium. If even one of the grains has more than six sides, then another grain with less than six sides would be created in order to maintain the average number of sides equal to six. Assuming the creation of a five sided grain, its internal angles are 108° when all its sides are of equal length. Therefore, the edges of this grain will become concave inwards in order to attain 120° angle at the vertex as shown in Fig. 13*b*. The angles in a seven sided grain are 128·57° when all its sides have the same length. The edges of this grain have to become concave outwards in order to attain 120° angle as shown in Fig. 13*b*. Now, once the grain boundaries are curved, they tend to migrate towards their centre of curvature in order to reduce the boundary surface area and hence minimise the surface energy. Therefore, the seven sided grain will grow and the five sided grain will shrink. The overall result of the boundary migration is to reduce the number of grains, thereby increasing the mean grain size and reducing the total grain boundary energy. Figure 14 shows[9] the shrinkage of a five sided grain. A five sided grain shown in Fig. 14*a*, on shrinking, leads to a 4-rayed vertex in Fig. 14*b*, as shown by the symbol I. The 4-rayed vertex, in turn, decomposes into two 3-rayed vertices in Fig. 14*c*, as shown by the symbols II and III, and the

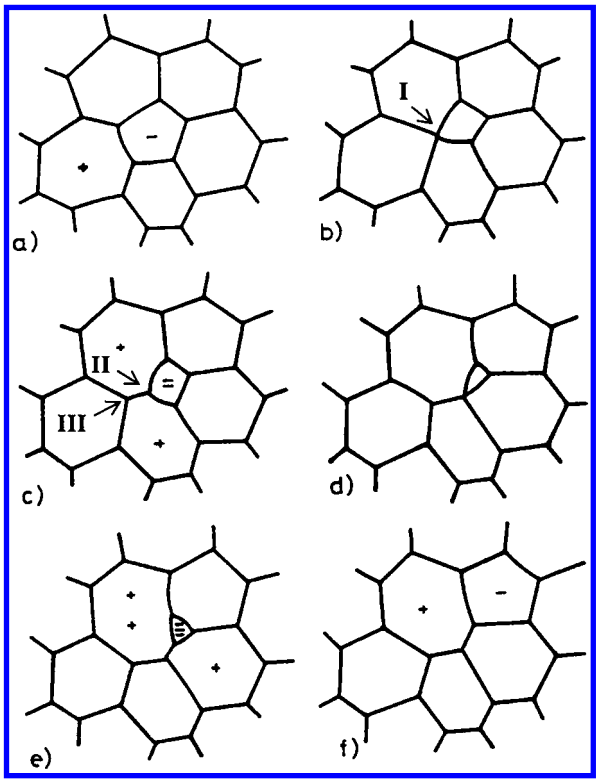

14 Two-dimensional grain structure illustrating instability when array does not consist of all regular hexagons: shrinkage of five sided grain to four sided grain followed by three sided grain and final disappearance, is clearly illustrated[9]

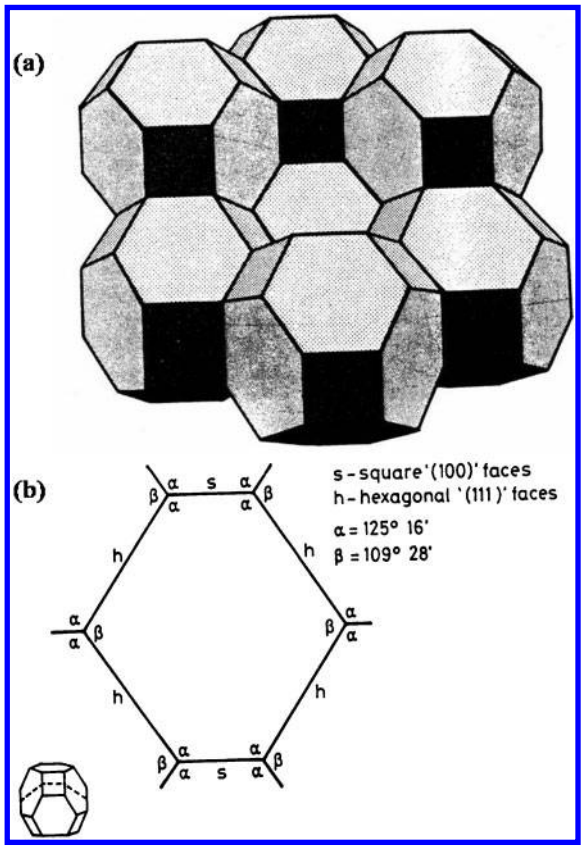

15 *a* group of regular tetrakaidecahedra[22] and *b* section through tetrakaidecahedron showing deviation from equilibrium angles[77]

five sided grain in Fig. 14*a* becomes four sided in Fig. 14*c*. The grain continues to shrink and undergoes a similar transformation to become three sided as shown in Fig. 14*d* and *e*. It then disappears completely, leaving a five sided grain neighbouring a seven sided grain, as shown in Fig. 14*f*. The foregoing example illustrates the influence of topological features of grains on grain growth.

In 3D, the nearest approach to space filling by a regular plane sided polyhedron is obtained with Kelvin tetrakaidecahedra[2,22] that are spaced on a body centred cubic lattice, as shown in Fig. 15*a*. For perfect space filling in 3D, tetrahedral angle 109°28′ should be formed between all the edges.[22] Even in this structure, the angles are not exactly tetrahedral[77] as shown in Fig. 15*b* and boundaries must become curved to achieve equilibrium at the vertices causing grain growth.

Analytical treatment of grain boundary migration

The soap froth example is often cited to understand the mechanism of the migration of a curved boundary. The higher pressure on the concave side of the soap films induces air molecules in the smaller cells to diffuse through the films in the larger cells.[5] Thus, the small cells eventually disappear. A similar effect occurs in metal grains. In the present case, the atoms in the shrinking grain detach themselves from the lattice on the high pressure side of the boundary and relocate on lattice sites of the growing grain. For example, in Fig. 16, if atom C jumps from grain 1 to grain 2 then the boundary locally advances a small distance from right to left.

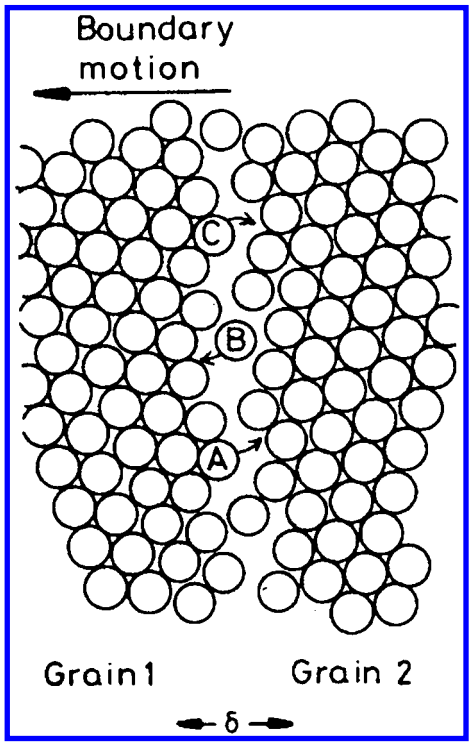

16 Atomic mechanism of boundary migration: boundary migrates to left if jump rate from grain 1 to grain 2 is greater than that from grain 2 to grain 1; free volume within boundary has been exaggerated for clarity[5]

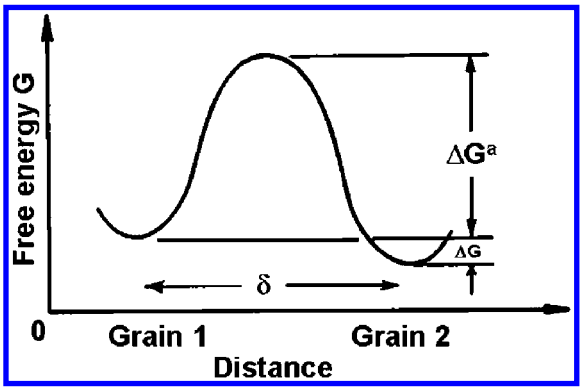

17 Free energy of atom during process of jumping from one grain to another[5]

The effect of the pressure difference caused by a curved boundary is to create a difference in free energy ΔG, as shown in Fig. 17, which drives the atoms across the boundary. In a pure metal, ΔG is given as[5]

$$\Delta G = \frac{2\gamma V_m}{r} \tag{6}$$

where γ is the grain boundary energy, V_m is the molar volume and r is the mean radius of curvature of the grain boundary assuming that it is a section of a sphere. This free energy difference can be thought of as a force pulling the grain boundary towards the centre of the grain with the higher free energy. The pulling force per unit area of boundary is given by[5]

$$P = \frac{\Delta G}{V_m} = \frac{2\gamma}{r} \tag{7}$$

in other words, the force per unit area on the boundary is simply the free energy difference per unit volume of the material.

By studying the effect of driving force per unit area P, on the kinetics of boundary migration, an expression for grain boundary velocity can be obtained. In order for an atom to be able to break away from grain 1, it must acquire, by thermal activation, an activation energy ΔG^a, as shown in Fig. 17. If the atoms vibrate with a frequency ν_1, the number of times per second N that an atom has this energy is[5]

$$N = \nu_1 \exp\left(-\frac{\Delta G^a}{RT}\right) \tag{8}$$

where R is the universal gas constant and T is the absolute temperature. If there are on an average n_1 atoms per unit area in a favourable position to make a jump, the number of jumps away from atom 1 N_1, is given by[5]

$$N_1 = n_1 \nu_1 \exp\left(-\frac{\Delta G^a}{RT}\right) \tag{9}$$

it is possible that not all these atoms will find a suitable site and 'stick' to grain 2. If the probability of being accommodated in grain 2 is A_2, the effective flux of atoms from grain 1 to grain 2 J_{12} (m^{-2} s^{-1}) is given by[5]

$$J_{12} = A_2 n_1 \nu_1 \exp\left(-\frac{\Delta G^a}{RT}\right) \tag{10}$$

there will also be a similar flux in the reverse direction, but if the atoms in grain 2 have a lower free energy than the atoms in grain 1 by ΔG, the flux from grain 2 to grain 1 J_{21} (m^{-2} s^{-1}) will be[5]

$$J_{21} = A_1 n_2 \nu_2 \exp\left(-\frac{\Delta G^a + \Delta G}{RT}\right) \tag{11}$$

when $\Delta G = 0$, the two grains are in equilibrium and there is no net boundary movement. Under this condition, the rates at which atoms cross the boundary in opposite directions must be equal. Equating J_{12} with J_{21}, the following equation is obtained[5]

$$A_2 n_1 \nu_1 = A_1 n_2 \nu_2 \tag{12}$$

for a high angle grain boundary it seems reasonable to expect that $A_1 = A_2 = 1$ (Ref. 5). Assuming this equality also holds for small non-zero driving forces with $\Delta G > 0$, there will be a net flux from grain 1 to grain 2 given by[5]

$$J_{net} = A_2 n_1 \nu_1 \exp\left(-\frac{\Delta G^a}{RT}\right)\left[1 - \exp\left(-\frac{\Delta G}{RT}\right)\right] \tag{13}$$

if the boundary moves with a velocity v ($m\ s^{-1}$), the velocity can be related to the net flux as[5]

$$J_{net} = \frac{v}{V_m / N_a} \tag{14}$$

where N_a is the Avogadro's number and V_m/N_a is the atomic volume. Then, using equations (13) and (14), expanding $\exp(-\Delta G/RT)$ as $[1-(\Delta G/RT)+(\text{higher order terms})]$, and neglecting the (higher order terms) because $\Delta G \ll RT$, gives[5]

$$v = \frac{A_2 n_1 \nu_1 V_m^2}{N_a RT} \exp\left(-\frac{\Delta G^a}{RT}\right) \frac{\Delta G}{V_m} = \mu P \tag{15}$$

where μ is the mobility of the boundary, i.e. the velocity under unit driving force and P is the driving force given in equation (7). Equation (15) shows that v should be proportional to the driving force P, and the mobility will increase spontaneously with temperature. This result, however, is intuitively obvious, because the boundary migration is a thermally activated process like diffusion. The only difference between the two is that the diffusion involves transport along the boundary, whereas the migration requires atomic movement across the boundary.

The expression for velocity in equation (15) can be simplified by making certain substitutions and assumptions. The activation energy ΔG^a can be written as $\Delta H^a - T\Delta S^a$, where ΔH^a is the activation enthalpy and ΔS^a is the activation entropy. The atomic vibration frequency ν is related to temperature as[13]

$$\nu = \frac{RT}{N_a h} \tag{16}$$

where h is the Planck's constant. The activation entropy of grain boundary migration ΔS^a can be assumed to be equal to the fusion entropy of the material ΔS^f, owing to similarity between the structure of grain boundaries and that of a liquid.[13] The mean radius of curvature r of all grain boundaries in equation (6) can be assumed to be equal to the mean radius of grains $\bar{R}$.[13] Combining equations (7), (15) and (16) and replacing the symbols A_2 by A, n_1 by Z, ν_1 by ν and ΔH^a by Q, the simplified equation for the boundary velocity can be written as[5,13]

$$v = \frac{2\gamma A Z V_m^2}{\bar{R} N_a^2 h} \exp\left(\frac{\Delta S^f}{R}\right) \exp\left(-\frac{Q}{RT}\right) \tag{17}$$

it is shown by equation (17) that the boundary velocity

increases exponentially with temperature T and decreases exponentially with the activation enthalpy Q. It will be shown subsequently that these two parameters are very important when considering relative rate of grain growth in different materials. A direct application of equation (17) can be seen in the HAZ of a weldment, which has steep temperature gradients. Because boundary mobility, and hence boundary velocity is strongly dependent on temperature as shown by equation (17), its value can vary across a large grain close to the fusion zone. Thus, different parts of a large grain have different propensities to grow. Thus, the growth of any individual grain experiencing a temperature gradient is retarded by the dominant more rapid growth of faster growing grains at higher temperature regions. This phenomenon is known as thermal pinning[49] and its origin can be explained by equation (17).

The data for different parameters used in equation (17) are available in the literature. Thus, the grain boundary velocities for different materials can be calculated and compared. For a given temperature T and average grain size $\bar{R}$, the higher the boundary velocity v, the faster the grain growth. Table 3 shows the computed values of boundary velocity for different materials.[6,15,76,78–80] Comparing the boundary velocity for iron, copper and aluminium for comparable temperatures and the same average grain size, the boundary velocity for iron is the smallest and that for aluminium is the largest. Thus, growth of grains will be the slowest in iron among these three metals. The computed results are confirmed by the experimental results of first five minutes of grain growth in iron[15] and copper[80] at 973 K. The average grain size in iron[15] increased from 50 to 80 μm, i.e. 60%, whereas, the average grain size in copper[80] increased from 10 to 49 μm, i.e. as much as 390%. It is noteworthy here that using a value of 50 μm for $\bar{R}$ for iron in equation (17) (in place of 10 μm as shown in Table 3) gives a value of v equal to $1{\cdot}42\times10^{-14}$ m s^{-1}, which is fairly close to the value in Table 3. The fourth and the fifth rows in Table 3 give the values of the boundary velocities for commercially pure titanium and its alloy Ti–6Al–4V respectively. The grain growth in alloys with low solute concentration is slower than that in the pure metal, because the solute elements hinder the migration of grain boundaries.[5] It can be seen that the calculated boundary velocity for the alloy is slower than that for the pure metal. Thus, equation (17) is able to predict the effects of various parameters on grain growth in different materials.

Burke and Turnbull[8] modelled grain boundary migration considering atom transport under pressure P, owing to surface curvature. Thus, the boundary velocity could be given in terms of P as in equation (15). The radius of curvature r, in equation (7), was assumed proportional to the average grain size $\bar{R}$. The boundary mobility μ was assumed independent of the average grain size. The grain boundary energy γ was assumed to be isotropic and independent of grain size and time. Furthermore, the rate of change of average grain size with time was assumed to be proportional to the pressure owing to surface curvature P, which drives the motion of the boundary. Based on the above assumptions, the radius of curvature r can be written as

$$r = C_1\bar{R} \tag{18}$$

where C_1 is a constant. Also, because $\mathrm{d}\bar{R}/\mathrm{d}t$ was assumed proportional to P, therefore

$$\frac{\mathrm{d}\bar{R}}{\mathrm{d}t} = C_2P \tag{19}$$

where C_2 is a constant. Thus, the dependence of average grain size of an array of grains on time can be expressed as

$$\frac{\mathrm{d}\bar{R}}{\mathrm{d}t} = \frac{2C_2\gamma}{C_1\bar{R}} \tag{20}$$

if $\bar{R}=\bar{R}_0$ at $t=0$ and $\bar{R}=\bar{R}_\mathrm{t}$ at $t=t$, the following expression is obtained by integrating equation (20)

$$\bar{R}_\mathrm{t}^2 - \bar{R}_0^2 = \frac{4C_2\gamma t}{C_1} \tag{21}$$

and hence

$$\bar{R}_\mathrm{t}^2 - \bar{R}_0^2 = Kt \tag{22}$$

where K is a constant. This parabolic grain growth equation is asserted to be valid for both two and three dimensions. If the diffusion of atoms across a grain boundary is considered to be an activated process, the constant K in equation (22) can be replaced by the expression[81]

$$K = K_0e^{-\mathrm{Q/RT}} \tag{23}$$

where Q is an empirical grain growth activation energy, T is the absolute temperature, and R is the universal gas constant. The grain growth equation, equation (22), can thus be written as a function of both temperature and time

$$\bar{R}_\mathrm{t}^2 - \bar{R}_0^2 = K_0te^{-\mathrm{Q/RT}} \tag{24}$$

this equation illustrates that higher the temperature for grain growth and larger the duration of growth, the larger the grain size. The effect of temperature on grain growth can be observed[82] from Fig. 18. As the temperature increases, the square of the average grain diameter $D^2=(2R)^2$ increases.[81] Furthermore, the activation energy Q, in equation (24), can be used to compare the rate of grain growth qualitatively in different materials. The higher the rate of grain growth in a material, the lower the value of Q. For example, as

Table 3 Physical and thermodynamic properties of various metals: first four entries in table have been taken from Ref. 79 where other data are taken from references mentioned in last column

Metal	$\bar{R}$, m	ΔH^a, J mol^{-1}	γ, J m^{-2}	ΔS^f, J mol^{-1} K^{-1}	V_m, m^3	Z, m^{-2}	T, K	v, m s^{-1}	Reference
Fe	1×10^{-5}	$2{\cdot}49\times10^5$	0·756	8·01	$7{\cdot}09\times10^{-6}$	$2{\cdot}0\times10^{19}$	973	$7{\cdot}11\times10^{-14}$	15
Cu	1×10^{-5}	$1{\cdot}27\times10^5$	0·625	9·48	$7{\cdot}11\times10^{-6}$	$2{\cdot}0\times10^{19}$	973	$2{\cdot}50\times10^{-7}$	80
Al	1×10^{-5}	$5{\cdot}80\times10^4$	0·324	5·90	$1{\cdot}00\times10^{-5}$	$1{\cdot}1\times10^{19}$	900	$2{\cdot}59\times10^{-4}$	6
β-Ti	5×10^{-5}	$1{\cdot}02\times10^5$	0·750	7·21	$1{\cdot}10\times10^{-5}$	$2{\cdot}0\times10^{19}$	1373	$9{\cdot}47\times10^{-5}$	78
β-Ti–6Al–4V	5×10^{-5}	$1{\cdot}70\times10^5$	0·700	7·21	$1{\cdot}10\times10^{-5}$	$2{\cdot}0\times10^{19}$	1373	$2{\cdot}29\times10^{-7}$	76

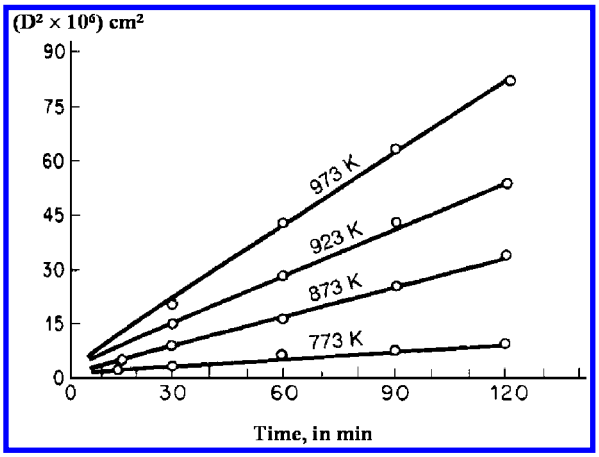

18 Grain growth isotherms for α-brass (10Zn–90Cu, wt-%): grain diameter squared D^2 varies linearly with time[82]

shown in Fig. 19, the growth kinetics of Ti–0·2Pd (wt-%) alloy is slower than that of pure β-titanium. This behaviour is consistent with the higher activation energy for the grain growth in the alloy, 56 kJ mol^{-1}, as compared with 21 kJ mol^{-1} for pure titanium.[83]

Analytical determination of grain growth in non-isothermal system

Initial attempts to model grain growth in the HAZ involved development of analytical equations.[42,49,84,85] One popular analytical method was proposed by Ashby and Easterling[42] and Ion *et al.*[85] based on the idea of integrating the parabolic grain growth kinetic equation

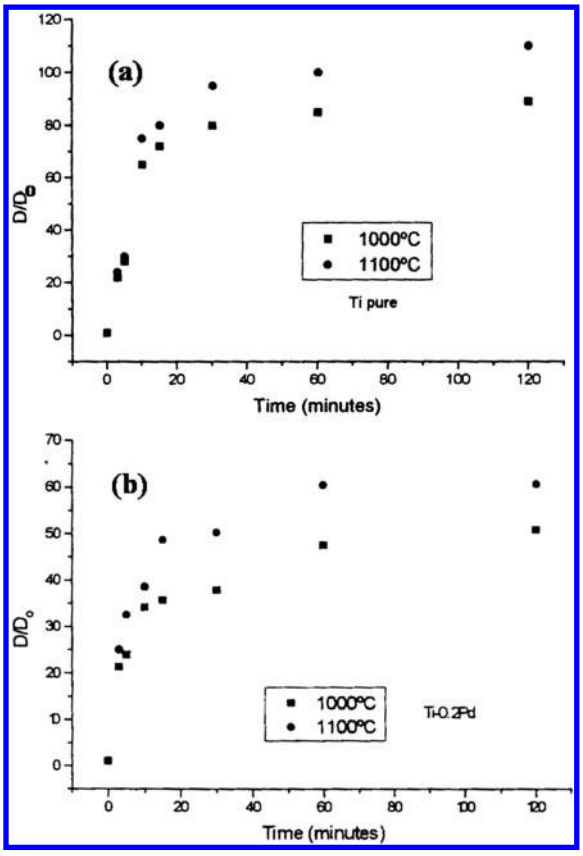

19 Ratio of diameters versus time of heat treatment in β phase region for *a* pure Ti and *b* Ti–0·2Pd alloy[83]

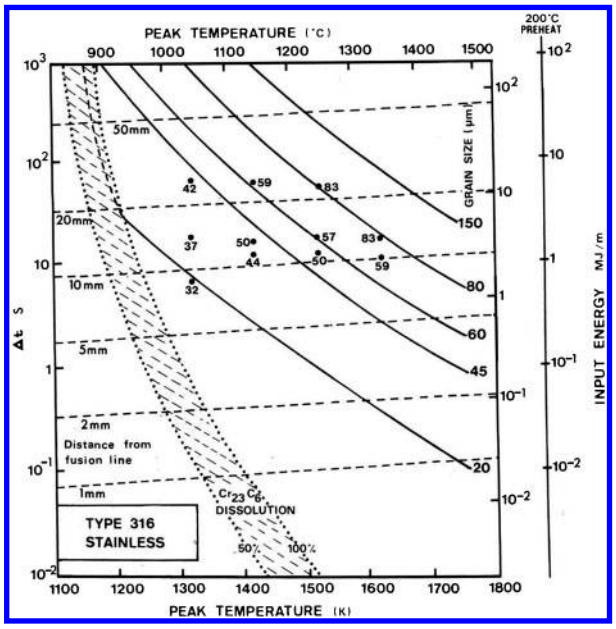

20 Diagram for AISI 316 austenitic stainless steel, constructed by fitting theory to experimental data[42]

(24) over weld thermal cycles calculated from the heat conduction equations. Ashby and Easterling[42] assumed that grain growth is driven by the reduction in grain boundary energy and requires no nucleation. Furthermore, grains were assumed to be spherical in shape. The austenite grain growth in the HAZ could be calculated by the following kinetic equation[42,85]

$$g^2 - g_0^2 = k_1 \int_0^{\infty} e^{-Q/RT(t)} \mathrm{d}t \qquad (25)$$

where g is the average grain size after time t, g_0 is the initial average grain size, k_1 is a kinetic constant, Q is the activation energy for grain growth, $T(t)$ is the temperature, which is a function of time, and R is the gas constant. For a specified material, the values of k_1 and Q need to be determined from experiments.

Ashby and Easterling[42] plotted experimental and calculated grain size data for six steels on different diagrams and showed the extent of grain growth for different heat input and at different points in the HAZ of welds. Figure 20 shows one such plot for 316 austenitic stainless steel. The y axis, on the left hand side, is the time Δt, for cooling between 800 and 500°C, which characterises the welding process. The input energy, in MJ m^{-1}, in the absence of any preheat, is given on the y axis on the right hand side. The x axis is the peak temperature T_p of the thermal cycle, which identifies a point in the HAZ. The solid dots represent the experimental data. The solid line contours of constant grain size were obtained by seeking, by trial and error, the value of Q in equation (25), which gave the best fit to the experimental data. The shaded band shows the range of dissolution of $Cr_{23}C_6$ particles, which pin grain growth. The 100% line is that at which dissolution of carbide is complete. The 50% line is that at which 50% carbide dissolves. The broken lines across the plot gave the distance of a location from the fusion line in mm. Thus, Fig. 20 can give the average grain size in the HAZ for a particular input energy, at a given distance from the fusion line. The second scale on the

right hand side shows the effect of preheat of 200°C. For a given T_p and input energy, the preheat causes an increase in grain size. Thus, the grain size plots prepared by Ashby and Easterling[42] summarise a large amount of data on the average grain size in the HAZ of welds in different steels. The spatial variation of grain size in the HAZ, and the change in average grain size with heat input and preheat can be estimated using these plots.

The analytical models for grain growth in non-isothermal systems have several limitations. The evolution of grain structure depends on various factors such as the orientations of the grains, the nature of the precipitates, the nature of the grain boundary network and the driving forces for boundary migration. The analytical equations do not account for all these factors in combination. Furthermore, grains in a polycrystal form a topologically connected network and the analytical models cannot fully consider the space filling requirement of a real grain structure. Also some special features of grain growth under non-isothermal conditions, such as 'thermal pinning' owing to steep temperature gradients, cannot be predicted by analytical calculations.[86] In recent years, significant progress has been made in the study of grain growth under non-isothermal conditions[45,67,72,87–103] using numerical techniques. These techniques can effectively model not only the kinetics of grain growth but also the evolution of the topological features of grain structure. The following sections describe the most common techniques and their applications.

Numerical calculations of non-isothermal grain growth

Available techniques

Common numerical techniques used for the calculation of non-isothermal grain growth include the CA technique, the MC method and the PF calculations. Table 4 shows a comparison of the salient features of these techniques. The CA technique simulates the evolution of grain structure by applying local physical rules at the cellular level and is deterministic in nature. Table 4 indicates that this technique has been mostly used for 2D simulation of grain growth during casting and hot rolling. The MC technique is a probabilistic technique where the evolution of grain structure is simulated by tracking the movement of the grain boundary driven by the reduction in grain boundary energy. It has been used for both 2D and 3D simulations of grain growth. The MC technique has been mostly applied to casting and the HAZ of welds. In the PF technique, the evolution of grain structure is governed by the Cahn–Hilliard nonlinear diffusion equation and the Allen Cahn relaxation equation. However, this technique has not been applied for simulating grain growth in non-isothermal systems. The detailed description of these techniques follows.

Cellular automaton

A CA technique is defined by four attributes, i.e. a collection of cells, the neighbourhood of a cell, the number of states a cell can attain and the rules of CA, which specify how the current states of the cells in the neighbourhood determine the next state of a cell. In the case of grain growth simulations using CA, the space is divided into a large number of individual cells and time is also discretised.[104–106] The state of each discrete cell is taken from a finite set of values that vary with time. The evolution of grain structure at different times is represented by the state of these individual cells. The neighbouring cells are defined as the cell itself and its surrounding cells at previous time step. In other words, the state of a cell at the time $t+\mathrm{d}t$ is only determined by the states of its neighbouring cells at time t. Von Neumann's definition of neighbourhood is commonly used for 2D calculations. As shown in Fig. 21*a*, the transition of states in 2D square cells is written as

$$x(i,j,t+\mathrm{d}t)= F[x(i,j,t),x(i,j+1,t),x(i+1,j,t),x(i-1,j,t),x(i,j-1,t)] \quad (26)$$

where $x(i,j,t)$ represents the states of ijth cell at time t. The function F embodies the transition rule, which

Table 4 Numerical techniques for non-isothermal grain growth calculations

	Cellular automaton (CA)	Monte Carlo (MC)	Phase field (PF)
Technique	Deterministic Tracks the interface Micrometre scale	Probabilistic Tracks the interface Micrometre as well as larger scales	Deterministic Does not track the interface Micrometre scale
	Describes grain structure in terms of cellular structure where each cell is defined as a phase	Describes grain structure in terms of random orientations	Describes grain structure using a set of conserved and non-conserved field variables that are continuous across the interfacial regions
	Evolution is governed by the local physical rules at the cellular level	Evolution is governed by the reduction of grain boundary energy	Evolution is governed by the Cahn–Hilliard nonlinear diffusion equation and the Allen Cahn relaxation equation
	Mostly 2D	Both 2D and 3D	Mostly 2D
Information obtained	Includes the effect of solute redistribution	Includes particle pinning, thermal pinning, grain boundary liquation pinning	Includes the influence of solute drag, effect of a dispersed phase in a matrix
	Gives temporal evolution of grain structure, predicts CET in casting	Gives temporal evolution of grain structure, grain size distribution, grain topology	Gives temporal evolution of grain structure, grain topology, grain size distribution
Applications	Castings, hot rolling and continuous cooling processes	HAZ of welds and castings	Binary alloy solidification during casting

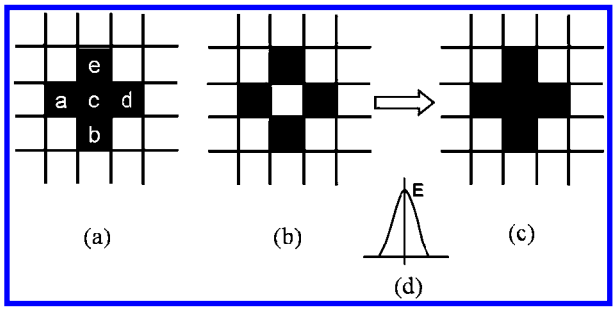

21 ***a*** **von Neumann's definition of neighbouring cells, cell c has a stable configuration as its state is same as state of three of its nearest neighbours,** ***b*** **cell at the centre is in a state depicted by white colour,** ***c*** **cell at centre changed its state from white colour to dark colour and** ***d*** **energy barrier** ***E*** **that the central cell in part** ***b*** **had to overcome to change its state to a dark colour shown in part** ***c*** [106]

forms the basis for boundary migration in CA. To illustrate the transition process, the following rules, based on grain growth theory and experiments, were used by Liu *et al.*[106] to simulate the normal grain growth:

(i) if three cells among the four surrounding cells a, b, d and e in Fig. 21*a* have the same state as the cell c, the state of the cell c will retain its original state at the next time step

(ii) a cell must overcome an energy barrier to reach its new state. In Fig. 21*b* the cell at the centre is in a state depicted by white colour. For this cell to attain a dark colour state as shown in Fig. 21*c*, an energy barrier E has to be overcome, which is shown in Fig. 21*d*

(iii) a cell can have states from 1 to $Q1$ ($Q1 \gg 1$). Each state represents the orientation of grain in a simulated microstructure. Random distribution of orientation is assumed during normal grain growth

(iv) grain boundary energy is homogeneously distributed.

This approach to simulate normal isothermal grain growth gives a basic foundation based on which the models for non-isothermal growth can be developed.

Rule (i) is a condition of stable configuration of a grain boundary. Here stable just means no change in state between the present and next time steps. Figure 22*a* shows the stable configuration, 'T' shape cluster with dark cells on the left side of the grain. In this case, the cell f can keep its state and the grain boundary on this side will not move at the next time step. On the other hand, a cell on the right side grain boundary, say cell g, has only two nearest neighbours that have the same state as cell g. As per rule (i), cell g is unstable and would try to attain a stable configuration. Thus, the right boundary is unstable and tends to migrate to the position of the broken line and form the stable configuration like that on the left side. This process is equivalent to the grain boundary migration owing to curvature effect shown in Fig. 22*b*. All the possible stable configurations in von Neumann's definition are shown in Fig. 22*c*. Rule (ii) is directly connected with temperature. According to statistical mechanics, the percentage of atoms, which can overcome an energy

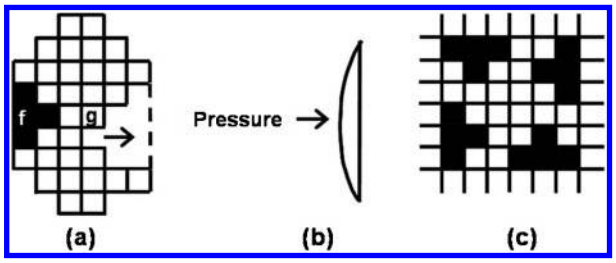

22 ***a*** **grain built by cells, unstable boundary on right side tends to migrate to position of broken line; cell f in stable configuration on left side of grain will keep its state in next time step; cell g on right grain boundary is unstable,** ***b*** **grain boundary migration owing to curvature effect and** ***c*** **all stable configurations in von Neumann's definition** [106]

barrier, is written as

$$P = \exp\left(-\frac{E}{kT}\right) \tag{27}$$

where E is the energy barrier, T the absolute temperature and k the Boltzmann constant. P also means the probability of successful transition of the state of a cell. Liu *et al.*[106] assumed a high enough temperature such that all the cells will be successful in their state transition, i.e. $P=1$. Rule (iii) is concerned with representation of grains. As in the MC simulation, described in the next section, a large value of the possible grain orientations or states $Q1$, allows to avoid the impingement of grains of like orientations.[10] Liu *et al.*[106] took $Q1$ as 1000. Rule (iv) is the nature of normal grain growth, which means that a cell can take the states of its neighbour at previous time with equal probability. The grain boundary is defined such that two cells with different states are separated by a minimum unit length of grain boundary. A time step was defined when all the cells underwent an attempt of state transition. Periodic boundary conditions were introduced in order to represent infinite microstructure. Using this model, Liu *et al.*[106] could effectively simulate the collapsing of an isolated circular grain in infinite matrix as well as the kinetics of normal grain growth, the grain size distribution and the topological class distribution.

The CA technique has been widely used for the simulation of grain growth under non-isothermal situations of casting, hot rolling and continuous cooling processes.[63,89–91,101,102] The isothermal CA model for grain growth is adapted to the non-isothermal systems by incorporating the relevant thermal cycles and defining a rule for updating the state of a cell based on the spatial and temporal variation of temperature. The applications will be discussed later in the paper.

Monte Carlo

The MC technique has been widely used to simulate grain growth[10–13,25,39–41,45,52,55,67,78,87,102,107–128] under both isothermal and non-isothermal conditions. This MC methodology for grain structure evolution is based on Potts[37] model. The model was first proposed by Potts[37] as a generalisation of the Ising[129] model for simulating the critical transitions in magnetic materials with more than two degenerate states. The Potts model treats the evolution of any non-equilibrium, discrete collection of entities that populate a grid. These entities can represent

the composition and structure of materials. An MC model for the simulation of grain growth under non-isothermal conditions[124] typically consists of the following tasks.

Defining initial grain structure

A computer image of the polycrystalline microstructure is first created by mapping the continuum grain structure on to a discrete lattice. This is accomplished by dividing the material into small volume elements and placing the centre of these elements on to the lattice points. The lattice may be simple cubic. Each of the grid points is assigned a random orientation number between 1 and $Q2$, where $Q2$ is the total number of grain orientations. A grain boundary segment is defined to lie between two sites of unlike orientation. In other words, two adjacent grid points with the same orientation number are considered to be a part of the same grain, otherwise they belong to different grains.

Defining the grain boundary energy

The grain boundary energy is specified by defining an interaction between the nearest neighbour lattice sites. The local interaction energy is calculated by the Hamiltonian[109]

$$E = -J\sum_{j=1}^{nn}(\delta_{s_i s_j} - 1) \tag{28}$$

where J is a positive constant which sets the scale of the grain boundary energy, δ is the Kronecker's delta function, S_i is the orientation at a randomly selected site i, and S_j are the orientations of its nearest neighbours. The sum is taken over all the nearest neighbour sites (nn). The nearest neighbour pairs contribute J to the system energy when they are of unlike orientation and zero otherwise.

The kinetics of grain boundary migration

the kinetics of grain boundary migration are simulated by selecting a site randomly and changing its orientation to one of the nearest neighbour orientations based on energy change owing to the attempted orientation change. The probability of orientation change is defined as[109]

$$p = 1 \quad \text{for} \quad \Delta E \leqslant 0$$
$$p = e^{-\frac{\Delta E}{k_B T}} \quad \text{for} \quad \Delta E > 0 \tag{29}$$

where ΔE is the change of energy owing to the change of orientation, k_B is the Boltzmann constant, and T is the temperature. Thus, a change in the orientation of a lattice site to an orientation of the nearest neighbour grain corresponds to boundary migration. The dimensionless grain size changes with the number of iterations, which is also known as the MC simulation time step t_{MCS}. Through the MC simulation, an empirical relation between the simulated grain size and the MC simulation time can be obtained as[109]

$$L = K_1 \times \lambda \times (t_{MCS})^{n_1} \tag{30}$$

where L is the dimensionless simulated grain size measured by mean grain intercepts, λ is the discrete grid point spacing in MC technique, K_1 is the simulated kinetic constant, and n_1 is the simulated value of the inverse of the grain growth exponent. Both K_1 and n_1 are the model constants, which are obtained by regression analysis of the data generated from MC simulation.

Relation between real time and t_{MCS} to apply MC kinetics to real systems

The grain size variation in the MC technique is largely independent of material properties and real time grain growth kinetics and is only dependent on the grid system. In order to quantitatively predict grain growth for a specific material under given thermal conditions, a relation needs to be established between the simulation steps t_{MCS} and real time. Therefore, a kinetic submodel is needed to simulate grain growth in real systems using the MC technique. Glazier *et al.*,[130] Radhakrishnan and Zacharia[86] and Saito and Enomoto[11] gave linear relations between t_{MCS} and real time. Gao and Thompson[13] argued that there was insufficient evidence to show that the MC simulation time could be linearly related to the real time in all material systems. They[13] proposed three models to relate t_{MCS} and real time for different situations. These were the atomistic model, the experimental data based (EDB) model and the grain boundary migration (GBM) model. The use of specific method depends on the nature of the problem.

In the atomistic model, the grid points in the simulated domain are treated as atoms. The MC simulation step is correlated to atomic diffusion across grain boundary and connected to real time temperature by the following relationship[125]

$$t_{MCS} = vt\exp\left(-\frac{Q}{RT}\right) \tag{31}$$

where v is the atomic vibration frequency, Q is the activation energy for grain growth, R is the gas constant, T is temperature and t is real time. To apply equation (31) to grain growth in a non-isothermal system, the thermal cycle experienced at a location is divided into many short intervals. The temperature in each time interval is assumed to be constant. The t_{MCS} for a thermal cycle is thus obtained by summation of the t_{MCS} at each time interval, which can be expressed as[125]

$$t_{MCS} = \sum_{i=1}^{m} v \times \exp\left(-\frac{Q}{RT_i}\right) \times \Delta t_i \tag{32}$$

where T_i is the average temperature within the time interval Δt_i and m is the number of time intervals. Because of the small size of the atoms and the limitation of computer resources, the atomistic model can only be used to simulate grain growth in a structure with small assemblies of atoms such as nanocrystals. To simulate grain growth associated with large grain size, the GBM and EDB models can be used. In these two models, the grid points are treated as blocks of physical volume in the material.

Grain boundary migration model utilises the concept that grain boundary migration reduces number of grains, thereby increasing the mean grain size and reducing the total grain boundary energy. Assuming that grain growth is driven by reduction in grain boundary energy and requires no nucleation, a simplified expression for the grain boundary migration velocity v is given by equation (17). Gao *et al.*[125] further assumed that the velocity of grain boundary migration is

related to the growth rate by the following relationship

$$v = \frac{\mathrm{d}(L/2)}{\mathrm{d}t} = \frac{1}{2} \times \frac{\mathrm{d}L}{\mathrm{d}t} \tag{33}$$

where L represents the average grain size $\bar{R}$. The grain boundary energy γ was assumed to be independent of grain size and grain orientation. Combining equations (17) and (33), incorporating the above assumptions and integrating over the range $L=L$ at $t=t$, and $L=L_0$ at $t=0$, the isothermal grain growth kinetics could be deduced as[125]

$$L^2 - L_0^2 = \frac{4\gamma AZV_{\mathrm{m}}^2}{N_{\mathrm{a}}^2 h} \times \exp\left(\frac{\Delta S^{\mathrm{f}}}{R}\right) \times \exp\left(-\frac{Q}{RT}\right) \times t \tag{34}$$

equating the mean grain intercept of equation (34) to that of equation (30) and integrating t_{MCS} over the entire thermal cycle, the t_{MCS} for simulation of grain growth could be expressed as[125]

$$(t_{\mathrm{MCS}})^{2n_1} = \left(\frac{L_0}{K_1\lambda}\right)^2 + \frac{1}{(K_1\lambda)^2}\left[\frac{4\gamma AZV_{\mathrm{m}}^2}{N_{\mathrm{a}}^2 h} \times \exp\left(\frac{\Delta S_{\mathrm{f}}}{R}\right)\right] \times \sum_{i=1}^{m}\left[\Delta t_i \times \exp\left(-\frac{Q}{RT_i}\right)\right] \tag{35}$$

using equation (35), the MC simulation time t_{MCS}, for a non-isothermal process can be related with its temperature time history. Mishra,[76] who used this expression to simulate grain growth in the HAZ of welds, suggested that if a single relation such as equation (30) is being used for calculating the t_{MCS} at all the sites in the HAZ, the initial grain size cannot be neglected. The relation between the average grain size L and the initial average grain size L', can be written as

$$L = L' + K_1 \times \lambda \times (t_{\mathrm{MCS}})^{n_1} \tag{36}$$

equation (36) represents the intrinsic grain growth kinetics of the MC model where L and t_{MCS} are dimensionless quantities. However, in the dimensionless growth kinetics of MC simulation, the initial average grain size L' has no relation to the actual initial average grain size L_0 of the material. The variable L' is set equal to the grid spacing λ for MC simulation.[76] Thus, equation (36) becomes

$$L = \lambda + K_1 \times \lambda \times (t_{\mathrm{MCS}})^{n_1} \tag{37}$$

equating the mean grain intercept of equation (34) to that of equation (37) and integrating over an entire thermal cycle, the revised relation for t_{MCS} for the GBM model becomes[76]

$$t_{\mathrm{MCS}} = \left\{\frac{1}{K_1\lambda}\left[\frac{4\gamma AZV_{\mathrm{m}}^2}{N_{\mathrm{a}}^2 h} e^{\Delta S_{\mathrm{f}}/R} \sum_{\mathrm{i}}\left(\Delta t_{\mathrm{i}} \exp\left(-\frac{Q}{RT_{\mathrm{i}}}\right)\right) + L_0^2\right]^{\frac{1}{2}} - \frac{1}{K_1}\right\}^{\frac{1}{n_1}} \tag{38}$$

where T_{i} is the mean temperature in a small time interval of duration Δt_{i}. Thus, at any monitoring location where the temperature is known as a function of time, t_{MCS} can be related to real time ($t=\Sigma\Delta t_{\mathrm{i}}$) using equation (38). Higher the temperature and longer the time for grain growth at a site, the higher is the value of t_{MCS} obtained from equation (38).

The EDB model is derived as follows. Based on the data from isothermal grain growth experiments, a relation can be established between the grain size L, temperature T and holding time t, which can be expressed as[125]

$$L^{\mathrm{n}} - L_0^{\mathrm{n}} = K \times t \times \exp\left(-\frac{Q}{RT}\right) \tag{39}$$

where n is the experimental grain growth exponent and K is the pre-exponential constant. Combining equations (30) and (39), the relation between the t_{MCS} for the isothermal grain growth and the real time temperature could be established as[125]

$$(t_{\mathrm{MCS}})^{n \times n_1} = \left(\frac{L_0}{K_1\lambda}\right)^{\mathrm{n}} + \frac{K}{(K_1\lambda)^{\mathrm{n}}} \times t \times \exp\left(-\frac{Q}{RT}\right) \tag{40}$$

for non-isothermal case, the temperature time curve in the HAZ is divided into many intervals and the temperature is assumed to be constant over each step. Equation (40) can then be transformed as

$$(t_{\mathrm{MCS}})^{n \times n_1} = \left(\frac{L_0}{K_1\lambda}\right)^{\mathrm{n}} + \frac{K}{(K_1\lambda)^{\mathrm{n}}} \times \sum_{i=1}^{m}\left[\Delta t_i \times \exp\left(-\frac{Q}{RT_i}\right)\right] \tag{41}$$

in equation (41), the t_{MCS} is related with real time temperature history based on available isothermal grain growth kinetic data n, Q and K. Mishra and DebRoy[52] suggested a revised equation for the EDB model based on an argument similar to the one given above for GBM model. The revised expression is

$$t_{\mathrm{MCS}} = \left\{\frac{1}{K_1\lambda}\left[K\sum_{\mathrm{i}}\left(\Delta t_{\mathrm{i}} \exp\left(-\frac{Q}{RT_{\mathrm{i}}}\right)\right) + L_0^{\mathrm{n}}\right]^{\frac{1}{\mathrm{n}}} - \frac{1}{K_1}\right\}^{\frac{1}{n_1}} \tag{42}$$

the GBM model is a good approach for grain growth simulation when the isothermal grain growth data for a given material are not available. However, the physical and thermodynamic properties of the material must be available. Strictly speaking, the GBM model is only valid for pure materials. This is because the value of grain growth exponent n is assumed to be 2·0 in the model, as shown in equation (38). This ideal value of 2·0 is theoretically derived and is only suitable for very pure materials at high temperatures, in which the effects of solute drag, impurity segregation, and second phase particles on grain growth can be ignored. Thus, for metals with relatively high content of impurities, or in alloys the EDB model should be used. However, the EDB model can only be used when sufficient kinetic data for isothermal grain growth at different temperatures are available.

Spatial gradient of temperature

An important feature of the MC technique to model grain growth is that in the MC technique, the choice of grid points for updating the grain orientation number is random. As a consequence, the probability to select each grid point is the same. However, grains must grow at faster rates in regions of higher temperatures and this fact must be included in the calculation scheme.

Therefore, the spatial gradient of temperature is represented by gradient of t_{MCS} which, in turn, is incorporated in the simulation by visiting each site with a probability p'[124]

$$P' = \frac{t_{MCS}}{t_{MCSMAX}} \tag{43}$$

where t_{MCS} is the computed MC simulation time at any site and t_{MCSMAX} is the maximum MC simulation time in the entire simulation domain. This way, locations with higher t_{MCS} and higher temperature are updated more frequently and the spatial gradient of temperature is properly taken into account.

Finally, after getting the calculated grain structure map from the MC simulations, the size and topological features of the grains can be readily calculated.

Phase field

The PF method has emerged as a powerful computational approach to modelling and predicting mesoscale morphological and microstructural evolution in materials. It describes a microstructure using a set of conserved and non-conserved field variables that are continuous across the interfacial regions. The temporal and spatial evolution of the field variables is governed by the Cahn–Hilliard nonlinear diffusion equation and the Allen Cahn relaxation equation.[118] With the fundamental thermodynamic and kinetic information as the input, the PF method is able to predict the evolution of arbitrary morphologies and complex microstructures without explicitly tracking the positions of the interfaces.[118]

In the last few years, the PF approach has been used to simulate grain growth under isothermal conditions both in the 2D and 3D.[118–120] However, it is very difficult and time consuming to consider non-isothermal situations in the PF approach,[94,121] primarily because of the difficulties in considering heat and mass transport calculations simultaneously with grain growth calculations. The 2D PF model for isothermal grain growth developed by Fan and Chen[119] and the more recent 3D version of the model developed by Krill and Chen[120] are described as follows. In the 2D phase field model for isothermal grain growth,[119] the microstructure of a polycrystalline simulation cell is specified by a set of $Q3$ continuous order parameters $\{\eta_q(r,t)\}$ $\{q = 1, 2, \ldots, Q3\}$ defined at a given time t at each position r within the simulation cell. The thermodynamics of the simulation algorithm are formulated such that the total free energy is minimised when, within each grain, one and only one order parameter takes on a value of 1, and all other order parameters have the value zero. Therefore, the orientation of a given grain can be specified by the index q of the order parameter η_q equal to unity in that grain's interior. Because the adjacent grains are distinguished by different q values, the values of two order parameters change continuously from 0 to 1 or vice versa across a grain boundary, as illustrated in Fig. 23. Because of this continuous variation, grain boundaries in the phase field model are diffuse, rather than sharp, as in most other coarsening models.[119] Inspired by Allen and Cahn's diffuse interface theory for antiphase domain boundaries,[122] Fan and Chen[119] proposed the following expression for the total free energy of a polycrystalline microstructure defined by a set of order parameters

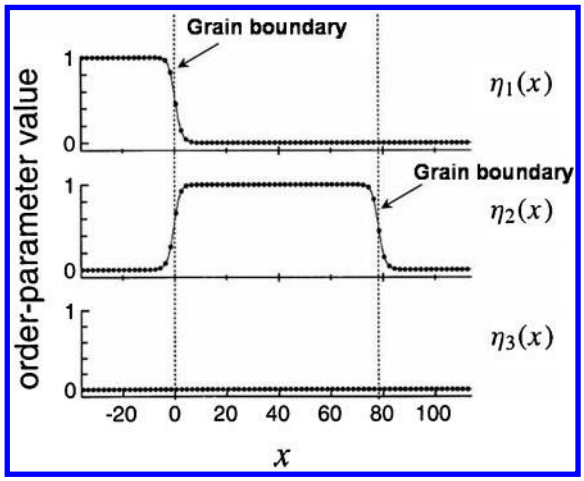

23 Section of 1D simulation grid illustrating values of order parameters η_1, η_2 and η_3 as function of position x: grain boundaries are regions of smooth variation in order parameter values between 0 and 1; location of centre grain between x=0 and x=80 is specified by η_2; owing to diffuse nature of grain boundaries in PF model,[119] values to left of x=0 and to right of x=80 must be included in order to retain smooth gradient following order parameter reassignment[120]

$$\{\eta_q(r,t)\}$$

$$F(t) = \int \left\{ f_0\left[\eta_1(r,t),\eta_2(r,t),\cdots,\eta_{Q3}(r,t)\right] + \sum_{q=1}^{Q3} \frac{\kappa_q}{2} \left[\nabla\eta_q(r,t)\right]^2 \right\} dr \tag{44}$$

where $\{\kappa_q\}$ are positive constants, and $f_0(\{\eta_q(r,t)\})$ denotes the local free energy density. The origin of the grain boundary energy comes from the gradient energy terms $(\nabla\eta_q(r,t))^2$. The smaller the gradient energy coefficient $\{\kappa_q\}$, the thinner the boundary region. If all the gradient energy coefficients are zero, the boundary becomes an infinitely thin, sharp interface. The local free energy density is defined as

$$f_0\left[\eta_q(r,t)\right] = -\frac{\alpha}{2}\sum_{q=1}^{Q3}\eta_q^2(r,t) + \frac{\beta}{4}\left(\sum_{q=1}^{Q3}\eta_q^2(r,t)\right)^2 + \left(\gamma - \frac{\beta}{2}\right)\sum_{q=1}^{Q3}\sum_{s>q}^{Q3}\eta_q^2(r,t)\eta_s^2(r,t) \tag{45}$$

in equation (45), α, β and γ are constants; for $\alpha=\beta>0$ and $\gamma>\beta/2$, f_0 has $2Q3$ degenerate minima located at (η_1, η_2, …, η_{Q3}) = (±1, 0, …, 0), (0, ±1, …, 0),…, (0, 0, …, ±1), which represent the equilibrium free energies of crystalline grains in 2Q3 different orientations. The minima associated with $\eta_q=-1$ can be eliminated as described below, leaving Q3 degenerate minima whenever one order parameter takes on the value of unity and the remaining order parameters are zero. Owing to the dependence of F on the square of the gradient of each order parameter, every unit of grain boundary area (i.e. a location of gradients in η_q) makes a positive contribution to the total free energy of the system. Therefore, there is a thermodynamic driving force for the elimination of grain boundary area, or, equivalently, for an increase in the average grain size. The reduction in free energy with time is assumed to follow the trajectory

specified by the set of variational derivatives of F with respect to each order parameter, which yield the time dependent Ginzburg–Landau equations[120]

$$\frac{\partial \eta_q(r,t)}{\partial t} = -L_q \frac{\delta F(t)}{\delta \eta_q(r,t)} (q = 1,2,\cdots,Q3) \quad (46)$$

$$= -L_q \left[-\alpha \eta_q(r,t) + \beta \eta_q^3(r,t) + 2\gamma \eta_q(r,t) \sum_{s \neq q}^{Q3} \eta_s^2(r,t) - \kappa_q \nabla^2 \eta_q(r,t) \right]$$

where $\{L_q\}$ are kinetic rate coefficients related to the grain boundary mobility. As described in the following section, equation (46) can be solved numerically at each lattice site to calculate the evolution of the microstructure.

After discretising equation (46) in both space and time, the forward Euler equation can be used to evaluate the values of the order parameters over a range of times at the site r of a regular lattice

$$\eta_q(r,t+\Delta t) = \eta_q(r,t) + \frac{\partial \eta_q(r,t)}{\partial t} \Delta t \quad (q = 1,2,...,Q3) \quad (47)$$

where $\partial \eta_q / \partial t$ is given by equation (46). The Laplacian operator of equation (46) is discretised as

$$\nabla^2 \eta_q(r,t) = \frac{1}{(\Delta x)^2} \sum_{i}^{1nn} \left[\eta_q(\gamma_i,t) - \eta_q(r,t) \right] \quad (48)$$

where the index i runs over all first nearest neighbour (1nn) sites $\{r_i\}$ to site r, and Δx is the uniform spacing between adjacent lattice sites. Periodic boundary conditions are imposed at the edges of the simulation grid. Starting from an initial state $\{\eta_q(r,0)\}$, equations (46)–(48) can be combined to solve iteratively for the order parameter values at integer multiples of the time step Δt.

It is convenient to specify the initial condition, i.e. the starting microstructure, by assigning a small random value $-0{\cdot}001 < \eta_q(r,0) < 0{\cdot}001$ to each order parameter at each site of the simulation lattice.[119] This state corresponds roughly to a supercooled liquid that will crystallise with increasing simulation time until the local free energy density f_0 at most sites assumes a minimum value, with only the sites located at the boundaries between grains making a positive relative contribution to the total free energy. The local minima of f_0 occur whenever a single order parameter takes on a value of either 1 or -1, and, in general, the crystallisation process leads to grains corresponding to both possibilities. Therefore, immediately following crystallisation, the simulation cell contains two distinct types of boundaries: the type illustrated in Fig. 23, across which η_j varies from 1 to 0 and $\eta_{k \neq j}$ from 0 to 1, and a second type, in which a single order parameter η_j varies from 1 to -1 or vice versa. The widths of these two boundary types differ slightly, which can lead to a difference in grain boundary mobility under the applied discretisation conditions. Therefore, in order to simulate the ideal case of uniform grain boundary mobilities and energies, one of the boundary types must be eliminated from the simulation cell. This can be accomplished by setting each order parameter equal to its absolute value, effectively restricting the available order parameter space to that containing only the Q3 degenerate minima of f_0 involving an order parameter equal to 1. In the simulations of Krill and Chen,[120] the absolute value operation was applied to the $\{\eta_q(r)\}$ values at $t = 15{\cdot}0$.

Visualisation of the simulated microstructure was aided by defining the function

$$\varphi(r,t) = \sum_{q=1}^{Q3} \eta_q^2(r,t) \quad (49)$$

which takes on a value of unity within individual grains and smaller values in the core regions of the boundaries. On mapping the values of φ to a spectrum of grey levels, Krill and Chen[120] obtained images of grain structure in which the grain boundaries appeared as dark regions separating individual grains. The topological properties of the grains, such as number of sides, cross-sectional area, or volume, could be evaluated directly by choosing a threshold value in φ to establish the boundary positions. In this manner, it was possible to quantify the evolution of local and averaged topological grain properties using the PF approach.

Table 5 compares the capabilities of experimental, analytical and numerical techniques in estimating the grain growth in non-isthermal systems. The much needed experimental tools for the characterisation of grain structure are now aided by newer numerical techniques, which allow realistic probing of 3D grain structure evolution. Table 5 indicates that although these models are complex as compared with the simple analytical models, their ability to quantitatively explain several special features of non-isothermal grain growth, such as the thermal pinning effect in HAZ and the CET in castings, has made them an important tool for probing grain growth in non-isothermal metallic systems.

Applications

The numerical techniques have been used to simulate grain growth in castings and in the HAZ of the welds. These applications are examined below.

Table 5 Comparison of available techniques for estimation of non-isothermal grain growth

	Experimental	Analytical	Numerical
Geometry	Both 2D and 3D	2D	Both 2D and 3D
Time taken	Large	Small	Medium
Information obtained	Temporal evolution of average grain size, actual grain size, grain size distribution, topological features	Temporal evolution of average grain size	Temporal evolution of grain structure, actual grain size, grain size distribution, grain topology, CET in castings
Features included	All physical processes	Pinning owing to the second phase particles	Pinning owing to the second phase particles, thermal pinning in HAZ
Limitations	Time consuming and tedious	Assumption of spherical grain shape is unrealistic	Requires highly complex and large computational efforts

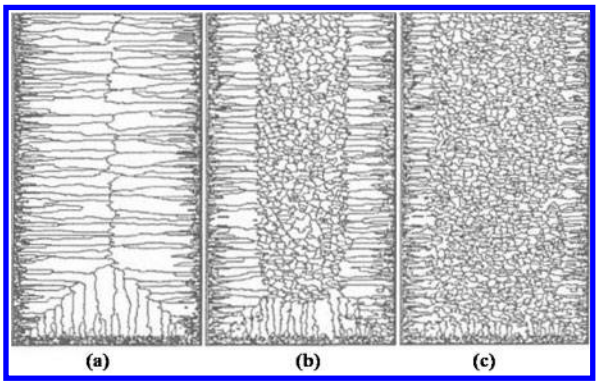

24 Effect of pouring temperature on macrostructure of ingots: simulations[98] used superheat temperatures of *a* 150°C, *b* 100°C and *c* 50°C

Grain growth during solidification of castings

Grain structure: several models for grain structure simulation during solidification have been developed in the recent years. Gandin and Rappaz[63] proposed an algorithm based upon 2D CA technique for the simulation of dendritic grain formation during solidification. The CA model took into account the heterogeneous nucleation, the growth kinetics and the preferential growth directions of the dendrites. It was applied to non-uniform temperature situations by coupling it with an enthalpy based finite element (FE) heat flow calculation model.[116] The calculated cooling curves agreed well with the experimental cooling curves measured with thermocouples. Gandin and Rappaz[63] applied the coupled CA–FE model to the 1D solidification of an Al–7Si (wt-%) alloy. The computed grain structure shown in Fig. 6*b* resembled the features of grain structure observed in the micrograph shown in Fig. 6*a*. The observed grain structure has been discussed in an earlier section of the present paper. Both Fig. 6*a* and *b* showed that the long columnar grains are formed first, followed by the formation of more equiaxed grains as the temperature gradient decreases. The presence of larger equiaxed grains near the top surface of the casting was also observed. Gandin and Rappaz[63] attributed some of the differences between the calculated and the experimental grain structures, like the difference in size of the equiaxed grains, to the use of a 2D CA grain growth simulation instead of a 3D model.

Zhu and Smith[97,98] developed a MC model to study the influence of pouring temperature on the solidification structure of an ingot of Al–4·5Cu (wt-%) alloy. In this model, the MC simulation was coupled with heat transfer and solute transfer equations. The interfacial energy and volumetric free energy were also taken into account. In order to demonstrate the influence of pouring temperature on the macrostructure of the ingot, various superheat temperatures were chosen. Figure 24 shows the simulation results. From these, Zhu and Smith[98] concluded that pouring temperature could have significant influence on the macrostructure and larger columnar zone was obtained with higher pouring temperature. This behaviour is observed in Fig. 24*a* which shows columnar grains and represents maximum superheat. The equiaxed grains form when the extent of superheat is reduced, as shown in Fig. 24*b* and *c*. A high pouring temperature reduces the 'shelter belt', i.e. the extent of undercooling in front of the solid/liquid interface, with consequent difficulty for equiaxed grains to form and grow. The simulation results[98] agreed with the general tendencies observed in experiments.

Spittle and Brown[100] developed a computer model for simulating the solidification of small castings using the MC technique. The model provided a pictorial representation of the as cast grain structure for any assumed set of solidification conditions and qualitatively predicted the experimentally observed influences of superheat, mould temperature, alloy composition and constitutional supercooling on grain structure. Increasing the superheat led to coarsening of the grain structure.

Wang and Beckermann[117] developed the Multiscale and Multiphase model, which was based on the volume averaging technique. As shown above, Spittle and Brown[100] and Zhu and Smith[97,98] established MC method based on the energy minimisation; and Gandin and Rappaz[63] developed the CA technique in which the physical mechanism of growth of dendritic grains was involved, and coupled it with the FE method. In order to take advantage of the strong features of all the above techniques simultaneously, Wang *et al.*[93] combined the CA technique and the MC method to simulate the grain structure of the solidified materials. The combined CA/MC model could predict the volume, size and the appearance of the grains better than either the CA technique or the MC method. In the growth algorithm, the CA technique accounted for the growth kinetics of the dendritic tips and for the preferential growth directions. However, the grain images simulated by this technique were slightly different from the normal grains obtained experimentally. The reasons were that the CA technique only adopts a deterministic equation to describe the grain shape, and does not account for the branching mechanisms of dendrite. In order to make up for the deficiency of the CA technique for the calculation of morphology, the MC method was used to correct the grain morphology. The MC method can simulate the random growth and the branching mechanism of dendrite growth while considering the effects of bulk free energy and interfacial energy. The CA/MC model[93] was applied to simulate the microstructural evolution of Al–4·5Cu (wt-%) alloy in water cooled Cu mould. The simulated results were in agreement with the final solidification structure obtained experimentally. Thus, the formation of the solidification structures could be simulated well by the CA/MC model.

Tsuta and Ivamoto[92] developed a 2D CA-MC-FE mathematical model of micromorphology generation during solidification. The heterogeneous nucleations from the wall and the grain growth kinetics were simulated using the MC technique. The finite element modelling (FEM) was used to solve the conventional heat transfer equation using appropriate boundary conditions. The morphologies obtained during solidification in a horizontal continuous casting apparatus were modelled. The simulated results were in good agreement with the experimental results for in vessel casting and twin roll casting of a two phase Al–Si alloy.

Columnar to equiaxed transition: the CET is of interest for understanding the mechanical properties of the solidified castings.[62] The CET is primarily governed by such casting parameters as the alloy composition, pouring superheat, nuclei density present in the melt, cooling capacity at the metal/mould interface and melt convection.[64] Qualitatively it can be anticipated that the

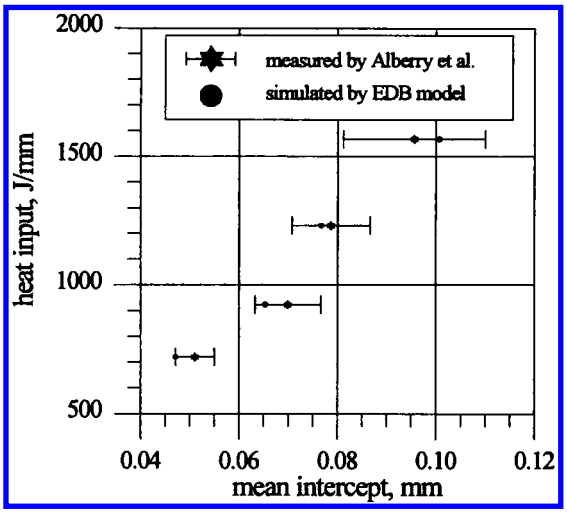

25 Comparison of experimental data[49] with simulated grain size in HAZ of 0·5Cr–Mo–V steel[125]

CET is facilitated when an alloy has a high solute level, low pouring temperature, small temperature gradient, high nuclei density present in the melt, and strong melt convection.[64] Wang and Beckermann[64] developed an approach to quantitatively predict the CET in alloy castings during dendritic solidification and confirmed the predictions with experiments. Only heat and solute diffusion was considered in the model; melt convection was neglected. The mathematical formulation was based upon a multiphase model.[115] The model distinguished the interdendritic and extradendritic liquid as two phases, by noting the fact that they are associated with two disparate interfacial length scales. A set of macroscopic equations governing solute diffusion was derived using the volume averaging procedure. The final model equations accounted for nucleation and growth of dendritic grains, dendrite morphology and both solute and heat diffusion. Given a realistic nucleation model, Wang and Beckermann's[64] model could provide good quantitative agreement between the measured and the calculated CET positions for several Sn–Pb and Al–Cu alloys for a wide variety of solidification conditions.

Vandyoussefi and Greer[91] used CA-FE simulations and Bridgman experiments to study the formation of equiaxed grain structures in directionally solidified Al–4·15Mg (wt-%) alloy. The model predicted a quasi-isothermal zone in directional solidification. This zone favours the formation of equiaxed rather than elongated grains. Both the experiments and the simulations confirmed observations that the CET occurs gradually, with the formation of short columnar or elongated grains intermitantly. All the above results indicate significant development and demonstrate the capabilities for the simulation of grain structures in castings.

Grain growth in HAZ of welds

The MC technique[52,55,76,78,86,109,123–125,131–133] has been used recently for modelling of grain growth in the HAZ. The MC technique can incorporate the 'thermal pinning' effect, which has been described previously in the paper. Both the size and topological features of the grains can be readily calculated from the final grain structure map obtained from the MC simulations.[10–12,52,76]

Grain structure: Gao *et al.*[125] used a 2D MC model to understand grain structure in three systems:

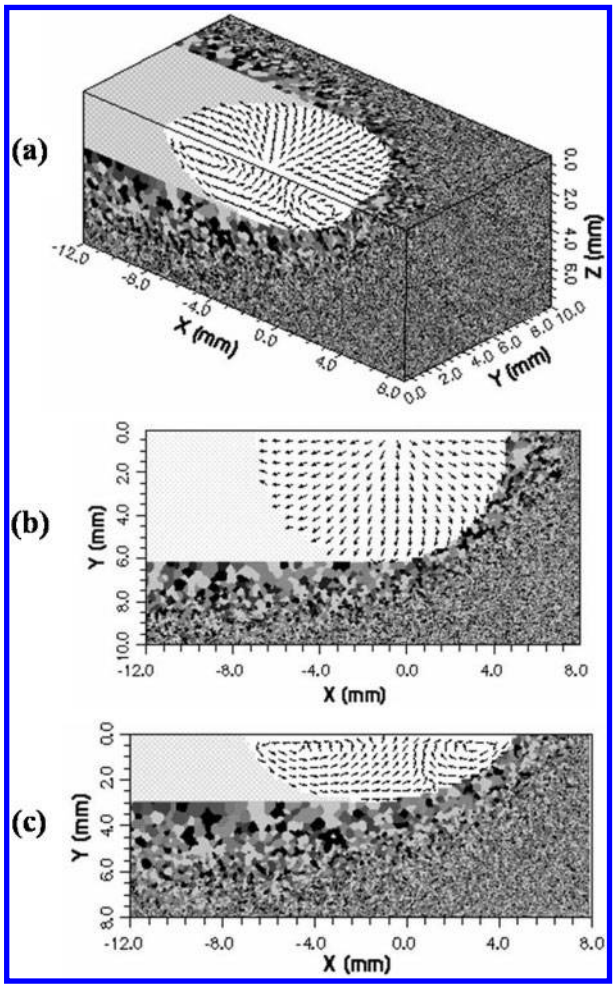

26 *a* real time mapping of grain structure distribution around weld pool in 3D using 400×200×160 grids: grid spacing is 50 μm; heat source is located at *x*= 0·0 and is moving from left to right, *b* top view of grain structure distribution around weld pool and *c* side view of grain structure distribution around weld pool[78]

(i) HAZ of a nanocrystalline nickel thin film heated by a low power continuous wave laser
(ii) a fillerless GTA butt weld in a pure aluminium plate
(iii) a 0·5Cr–Mo–V steel weld.

Depending on the material system investigated, different relations between the t_{MCS} and the real time were used. Because of the atomic scale thickness of the nanocrystalline nickel thin film, atomistic model was applied to couple MC simulation to atomic diffusion across grain boundaries in this system. As isothermal grain growth data[49] were available for 0·5Cr–Mo–V steel, an EDB model was used. The GBM model was used for the aluminium plate, because physical properties were available. The simulated average grain size[125] matched well with independent experimental results, as shown for the HAZ of 0·5Cr–Mo–V steel weld in Fig. 25. Sista *et al.*[109] used a 3D MC model to simulate the effect of heat input on grain growth in the HAZ of 2·25Cr–1Mo steel weld, and found good agreement between the calculated and the independent experimental[134] results.

Figure 26*a* shows a computed 3D map of β-titanium grain structure distribution around the weld pool.[78] A 3D MC model was used for these calculations.[78] The

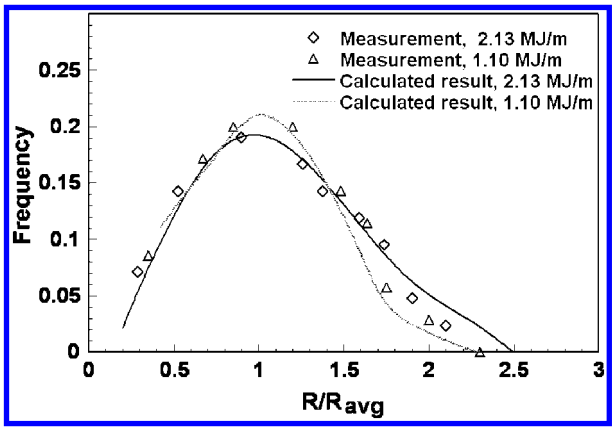

27 **Experimental and calculated grain size distributions at 1 mm from fusion plane on midsection vertical symmetry plane for heat inputs of 1·10 and 2·13 MJ m^{-1} (Ref. 52)**

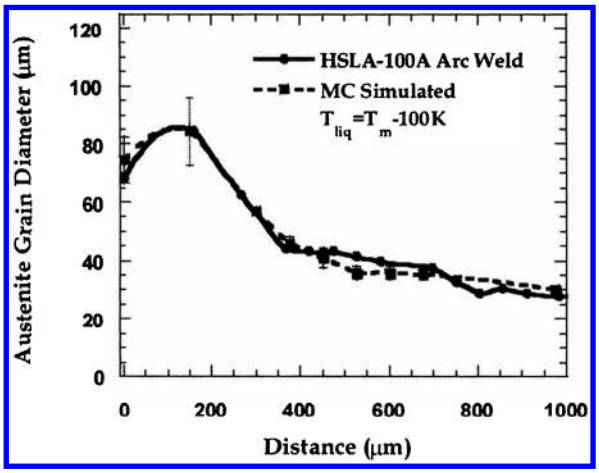

28 **Austenite grain size distribution for experimental HSLA-100 arc weld and MC simulated HAZ considering pinning owing to grain boundary liquation[123]**

model used thermal cycles computed from a well tested numerical 3D heat transfer and fluid flow model.[135–138] In the simulated grain structure map, the thermal effects on grain growth in the HAZ can be observed. In the region in front of the weld pool, the extent of grain growth was limited and the grain size was small owing to the very short time available for grain growth prior to melting. Behind the heat source in the solid region, the grains continued to grow until the temperatures reached the β–α transition temperature. Simultaneously, the width of the HAZ increased with time. These features could be seen from the top and side views of the simulated grain structure map shown in Fig. 26*b* and *c*. Significant spatial variation of grain size could be observed in the simulated HAZ structure. The closer a site to the fusion plane, the coarser the grain size at that site. This is expected because the grain size change depends on both the temperature and the time period for grain growth. The higher the temperature and the longer the time for grain growth, the larger the final grain size. Furthermore, it was observed that grain growth on the top surface of the HAZ in Fig. 26*b* was not as significant as that in the side view showing the symmetry plane in Fig. 26*c*. This difference originates from the local variation of thermal cycles which is one of the main factors that affects grain growth in the HAZ. Sista *et al.*[109] showed that these spatial variations of grain size cannot be accurately predicted using a 2D MC model, because accurate calculation of grain structure require consideration of space filling requirements in 3D and spatial gradients of temperature in all directions.

Mishra and DebRoy[52] investigated the grain size distributions in the HAZ for different heat inputs, i.e. distributions under the influence of different thermal cycles in Ti–6Al–4V alloy welds, as shown in Fig. 27. They[52] observed that the distributions were fairly identical, i.e. unaffected by the difference in thermal cycles. They[52] suggested that such a behaviour could be explained from the fact that any thermal cycle in the HAZ could be viewed as a collection of a large number of discrete isothermal steps applied for different times. Therefore, the grain size distribution under different thermal cycles behaved in a similar manner as that under different isothermal conditions[10,12,15] for different times, i.e. remained invariant.

Wilson *et al.*[123] observed that although the thermal pinning phenomenon had been simulated by the MC technique in the HAZ of 0·5Cr–Mo–V weld, the predicted grain size from the MC simulation was still larger than that observed in the actual weld HAZ especially in the regions close to the fusion zone. This indicated that there was an additional inhibition effect besides the 'thermal pinning'. They[123] believed that the formation of the grain boundary liquid was responsible for this additional pinning. The liquid in the HAZ may be formed by different mechanisms. The grain boundary liquid could be formed by the subsolidus liquation caused by the presence of soluble second phase particles[86,123,139] or by intergranular penetration of liquid and/or solute from the fusion zone along grain boundaries in the HAZ.[86] The dominance of one mechanism over another depends on the system investigated. The pinning effect owing to the liquation of grain boundary was simulated using MC technique by Wilson *et al.*[123] Because the grain growth was assumed completely pinned by the grain boundary liquid, a portion of the thermal cycle was not considered in the calculation of the MC simulation step t_{MCS} in the simulations. Thus, the t_{MCS} value and the simulated grain size near the fusion line decreased as the liquidus temperature decreased. Figure 28 shows that the simulated grain size was in good agreement with the experimental measurements. In this way, the effect of grain boundary liquidation on grain growth could be simulated by the MC technique.

Grain topology: the importance of grain topology has been well recognised in isothermal systems.[10–12,15,22,23,34,40,140–147] However, not much effort has been made to understand how the grain topology evolves under the influence of strong spatial and temporal variation of temperature. Mishra and DebRoy[55] studied the individual effects of the temperature gradient as well as the thermal cycles on the grain topology in the HAZ. Figure 29*a* shows the topological class distributions, i.e. the proportion of grains with specific number of sides (frequency) versus the number of sides, at two monitoring locations where the thermal cycles were significantly different, but the dominant temperature gradients were the same.[55] The topological class distributions were the same at both the locations indicating that the changes in the thermal cycles do not

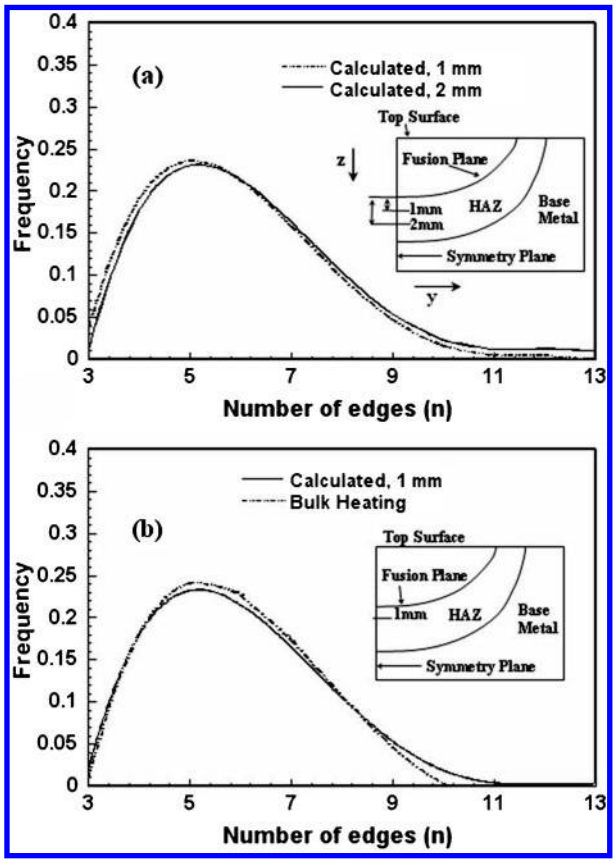

29 ***a*** **calculated topological class distributions at two monitoring locations in HAZ of Ti–6Al–4V weld that experience same temperature gradient but different thermal cycles: distributions are for locations 1 and 2 mm from fusion plane on midsection vertical symmetry plane for heat input of 4·33 MJ m^{-1}; because area is needed to determine grain structure and topological features, results from strip ±250 μm on either side of monitoring location were used and** ***b*** **calculated topological class distributions for two systems, both undergoing same thermal cycle but different temperature gradients: one distribution is for monitoring location 1 mm from fusion plane in HAZ on midsection vertical symmetry plane for heat input of 2·13 MJ m^{-1}; temperature gradient at this location is 164 K mm^{-1} and peak temperature of thermal cycle is 1714 K; other distribution corresponds to situation where entire calculation domain was subjected to same thermal cycle as that experienced at monitoring location in HAZ[55]**

affect the topological class distributions. Furthermore, the topological class distributions show the same attributes as those observed during normal grain growth under isothermal condition. Figure 29*b* shows the topological class distributions in two systems undergoing the same thermal cycle but one with significant spatial gradient of temperature, i.e. the HAZ of weld and the other without it, i.e. bulk heating.[55] The similarity of the two topological class distributions indicated that the distribution is unaffected by the temperature gradient. Thus, the topological class distribution was unaffected by both the thermal cycles and the temperature gradients in the HAZ. As shown in Fig. 2, for two systems experiencing the same thermal cycle but significantly different temperature gradients,

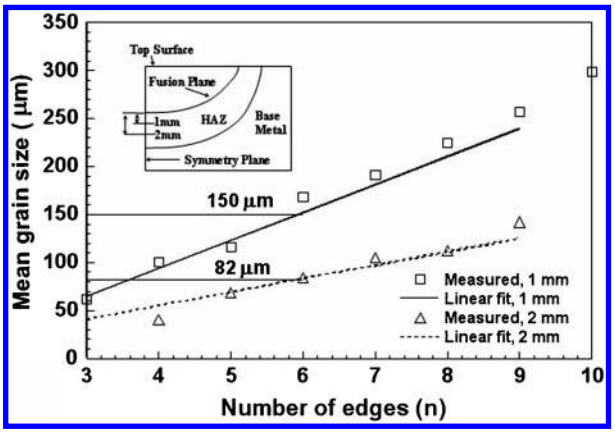

30 Mean grain size versus number of edges at distance of 1 and 2 mm from fusion plane on midsection vertical symmetry plane for heat input of 1·10 MJ m^{-1}: symbols represent experimental data while lines represent linear fit to calculated results; temperature gradient at two locations is 197 K mm^{-1}, and peak temperature of thermal cycle for 1 mm location is 1681 K and that for 2 mm location is 1484 K[55]

the grain size is much smaller under higher temperature gradient. This is due to the thermal pinning effect, which has been described in an earlier section of the present paper.

Figure 30 shows that the average grain size for each edge class increases linearly with the edge class number (number of sides) indicating that grains with larger number of sides grow faster.[52,55] The horizontal broken lines in Fig. 30 represented the average grain size at the respective locations. Thus, grains of average size had six sides, which is the average number of sides of grains at any location. Good agreement was observed between the calculated and the experimental results indicating that the MC model could accurately predict both size and topological features of grains in the HAZ of the alloy.

Summary and research needs

Grain growth in materials under significant spatial and temporal variations of temperature exhibits many special characteristics that cannot be understood from isothermal studies. Although significant progress has been made in understanding of various aspects of non-isothermal grain growth in metals and alloys, much needed improved understanding of many special features of non-isothermal grain growth represents both a major challenge and an exciting opportunity.

Much of the progress in the last several decades has been possible because of significant advances in numerical modelling capability and to a much lesser extent, in the characterisation of grain structure. A notable exception is the emerging experimental technique for non-contact, real time determination of average grain size through the application of laser induced ultrasonic waves. However, application of this non-contact, real time, tool for grain size measurement in various important engineering alloys must await considerable future work. In addition to the new knowledge generated by experimental characterisation of grain structure, the emerging suite of numerical tools now allow realistic probing of grain structure evolution in 3D. These models are large and complex, lack the elegance, clarity

and simplicity of the analytical models, and demand exceptional perseverance and skill for their development. However, their ability to quantitatively explain several hitherto unexplained special features of non-isothermal grain growth through consideration of realistic complex physical processes have already made them an important tool for probing grain growth in non-isothermal metallic systems. Many examples of their application have been included in the previous sections, but only two are mentioned here to remind readers that the efforts needed to develop these highly complex, large and numerical models are sometimes rewarded by new insights that cannot be obtained otherwise. Thermal pinning of grain growth in the HAZ of welds was proposed by Alberry *et al.*[49] However, it was not until a comprehensive 3D grain growth model was available that the phenomenon could be quantitatively demonstrated. Similarly, although the principle of the CET is well known, only through the application of complex numerical models, the CET and the relative volume fractions of the columnar and equiaxed grains could be predicted.

Monte Carlo technique has been very effectively applied to the modelling of grain growth in the HAZ where steep temperature gradients and variable thermal cycles offer unique conditions for grain growth. Both the size and topological features of grains have been quantitatively predicted, and the results have provided better understanding of grain growth in the HAZ. Coupled CA, MC and FE models have been successfully used to simulate the solidified casting grain structure consisting of both columnar and equiaxed grains. The termination of columnar growth owing to the formation of equiaxed grains and the subsequent growth of equiaxed grains have been modelled. The CET temperatures have been accurately predicted. The significant acceleration of grain growth under the influence of cyclic annealing, where rapid heating and cooling takes place, has been studied experimentally. Cellular automaton and MC techniques have provided significant insight about the evolution of grain structure that could not have been attained otherwise.

Although significant progress has been made, new important problems have also become apparent. For example, it is well known that the grain growth in cyclic annealing is faster than that during isothermal heating at the highest temperature of the thermal cycle. However, the mechanism of the enhanced grain growth during cyclic annealing remains to be adequately understood. Much of the complexity in the non-isothermal grain growth originates from the inherent structural features of metallic materials such as phase transformations and the dissolution and growth of precipitates, inclusions and other defects. Often the evolution of grain structure during processing of metallic materials is significantly affected by the dissolution and growth of precipitates and other defects, and the phase transformations that occur at high temperatures. Although some work has been performed in incorporating macroscopic defects in the quantitative understanding of grain growth in relatively simple cases, this problem needs considerable further study because of its complexity. Better understanding of the growth and dissolution of second phase particles and defects is needed for more reliable, quantitative understanding of grain structure evolution.

In addition to the MC and CA models, PF models have also evolved significantly in recent years. However, they have so far been applied in simpler 2D systems. Their application to 3D non-isothermal systems would require incorporation of complex heat and mass transport rates into the calculations. The existing models of grain growth have been applied to only a few important engineering alloys under non-isothermal conditions. As more systems are investigated, there will be progress towards developing a more extensive quantitative knowledge base in understanding grain growth under non-isothermal conditions. Significant expansion of the current knowledge base is needed for quantitative understanding of grain structure evolution in metals and alloys during their processing.

Acknowledgements

The present study was supported by a grant from the US Department of Energy, Office of Basic Energy Sciences, Division of Materials Sciences, under grant number DE-FGO2-01ER45900. The authors thank Mr W. Zhang, Mrs X. He, Mr A. Kumar, Dr C.-H. Kim and Dr A. De for their support during the preparation of this manuscript.

References

1. P. A. Beck: *Philos. Mag. Suppl.*, 1954, **3**, 245.
2. H. V. Atkinson: *Acta Metall.*, 1988, **36**, 469.
3. V. Novikov: 'Grain growth and control of microstructure and texture in polycrystalline materials', 1997, Boca Raton, FL, CRC Press.
4. T. Gladman: 'Grain size control'; 2004, London, Maney Publishing.
5. D. A. Porter and K. E. Easterling: 'Phase transformations in metals and alloys'; 1981, New York, van Nostrand Reinhold Company.
6. P. Feltham: *Acta Metall.*, 1957, **5**, 97.
7. P. A. Beck, J. C. Kremer, L. J. Demer and M. L. Holzworth: *Trans. AIME*, 1948, **175**, 372.
8. J. E. Burke and D. Turnbull: *Prog. Met. Phys.*, 1952, **3**, 220.
9. M. Hillert: *Acta Metall.*, 1965, **13**, 227.
10. D. J. Srolovitz, M. P. Anderson, P. S. Sahni and G. S. Grest: *Acta. Metall.*, 1984, **32**, 793.
11. Y. Saito and M. Enomoto: *ISIJ Int.*, 1992, **32**, 267.
12. S. Sista and T. DebRoy: *Metall. Mater. Trans. B*, 2001, **B32**, 1195.
13. J. Gao and R. G. Thompson: *Acta Mater.*, 1996, **44**, 4565.
14. P. Gordon and T. A. El-Bassyouni: *Trans. Metall. Soc. AIME*, 1965, **233**, 391.
15. H. Hu: *Can. Metall. Q.*, 1974, **13**, 275.
16. E. L. Holmes and W. C. Winegard: *Acta Metall.*, 1959, **7**, 411.
17. J. P. Drolet and A. Galibois: *Acta Metall.*, 1968, **16**, 1387.
18. F. J. Gil and J. A. Planell: *Mater. Sci. Eng. A*, 2000, **A283**, 17.
19. F. X. Gil, D. Rodriguez and J. A. Planell: *Scr. Metall. Mater.*, 1995, **33**, 1361.
20. F. J. Gil and J. A. Planell: *J. Mater. Sci. Lett.*, 2000, **19**, 2023.
21. G. F. Bolling and W. C. Winegard: *Acta Metall.*, 1958, **6**, 283.
22. C. S. Smith: 'Metal interfaces', 65; 1952, Materials Park, OH, ASM International.
23. J. von Neumann: 'Metal interfaces', 108; 1952, Materials Park, OH, ASM International.
24. N. P. Louat: *Acta Metall.*, 1974, **22**, 721.
25. M. P. Anderson, D. J. Srolovitz, G. S. Grest and P. S. Sahni: *Acta Metall.*, 1984, **32**, 783.
26. J. E. Morral and M. F. Ashby: *Acta Metall.*, 1974, **22**, 567.
27. N. F. Rhines and K. R. Craig: *Metall. Trans. A*, 1974, **A5**, 413.
28. R. D. Doherty: *Metall. Trans. A*, 1975, **A6**, 588.
29. O. Hunderi: *Acta Metall.*, 1979, **27**, 167.
30. V. Y. Novikov: *Acta Metall.*, 1978, **26**, 1739.
31. F. H. Rhines and B. R. Patterson: *Metall. Trans. A*, 1982, **A13**, 985.
32. O. Hunderi, N. Ryum and H. Westengen: *Acta Metall.*, 1979, **27**, 161.

33. E. A. Ceppi and O. B. Nasello: *Scr. Metall.*, 1984, **18**, 1221.
34. V. E. Fradkov, M. E. Glicksman, M. Palmer and K. Rajan: *Acta Metall. Mater.*, 1994, **42**, 2719.
35. D. Fan and L. Q. Chen: *Acta Mater.*, 1997, **45**, 611.
36. S. M. Allen and J. W. Cahn: *Acta Metall.*, 1979, **27**, 1085.
37. R. B. Potts: *Proc. Camb. Philol. Soc.*, 1952, **48**, 106.
38. E. A. Holm, J. A. Glazier, D. J. Srolovitz and G. S. Grest: *Phys. Rev. A*, 1991, **A43**, 2662.
39. G. S. Grest, M. P. Anderson and D. J. Srolovitz: *Phys. Rev. B*, 1988, **B38**, 4752.
40. M. P. Anderson, G. S. Grest and D. J. Srolovitz: *Philos. Mag. B*, 1989, **B59**, 293.
41. S. Ling and M. P. Anderson: *JOM*, 1992, **44**, 30.
42. M. F. Ashby and K. E. Easterling: *Acta Metall.*, 1982, **30**, 1969.
43. J. W. Martin and R. D. Doherty: 'Stability of microstructure in metallic systems', 228; 1976, New York, Cambridge University Press.
44. R. A. Vandermeer and H. Hu: *Acta Metall. Mater.*, 1994, **42**, 3071.
45. S. S. Sahay, C. P. Malhotra and A. M. Kolkhede: *Acta Mater.*, 2003, **51**, 339.
46. S. A. David and T. DebRoy: *Science*, 1992, **257**, 497.
47. T. DebRoy and S. A. David: *Rev. Mod. Phys.*, 1995, **67**, 85.
48. M. Vandyoussefi and A. L. Greer: *Acta Mater.*, 2002, **50**, 1693.
49. P. J. Alberry, B. Chew and W. K. C. Jones: *Met. Technol.*, 1977, **4**, 317.
50. P. J. Alberry and W. K. C. Jones: *Met. Technol.*, 1977, **4**, 557.
51. K. Easterling: 'Introduction to the physical metallurgy of welding'; 1983, London, UK, Butterworths.
52. S. Mishra and T. DebRoy: *Acta Mater.*, 2004, **52**, 1183.
53. T. George and J. J. Irani: *J. Aust. Inst. Met.*, 1968, **13**, 94.
54. S. Matsuda and N. Okumura: *Trans. ISIJ*, 1978, **18**, 198.
55. S. Mishra and T. DebRoy: *J. Phys. D: Appl. Phys.*, 2004, **37**, 2191.
56. C. A. Schuh and D. C. Dunand: *Acta Mater.*, 2002, **50**, 1349.
57. H. Geng, S. He and T. Lei: *Metall. Mater. Trans. A*, 1997, **A28**, 1809.
58. R. S. Yang: *Heat Treat. Met.*, 1993, **1**, 32.
59. D. V. Andreev, V. N. Bespalov, A. Y. Biryukov and E. A. Krasikov: *J. Nucl. Mater.*, 1999, **274**, 329.
60. E. A. Smolnikov and L. M. Orestova: *Met. Sci. Heat Treat.*, 1982, **24**, 519.
61. S. S. Kim and D. N. Yoon: *Acta Metall.*, 1983, **31**, 1151.
62. B. Chalmers: 'Principles of solidification', 1964, New York, John Wiley.
63. C.-A. Gandin and M. Rappaz: *Acta Metall. Mater.*, 1994, **42**, 2233.
64. C. Y. Wang and C. Beckermann: *Met. Mater. Trans. A*, 1994, **A25**, 1081.
65. S. G. R. Brown and J. A. Spittle: *Mater. Sci. Technol.*, 1989, **5**, 362.
66. M. Militzer, A. Giumelli, E. B. Hawbolt and T. R. Meadowcroft: *Metall. Mater. Trans. A*, 1996, **A27**, 3399.
67. M. J. Leap and E. L. Brown: *Mater. Sci. Technol.*, 2002, **18**, 945.
68. M. Dubois, A. Moreau, M. Militzer and J. F. Bussiere: *Scr. Mater.*, 1998, **39**, 735.
69. M. Dubois, M. Militzer, A. Moreau and J. F. Bussiere: *Scr. Mater.*, 2000, **42**, 867.
70. S. Kruger, A. Moreau and G. Lamouche: Proc. 1st Joint Int. Conf. on 'Recrystallization and grain growth', (ed. G. Gottstein and D. A. Molodov), 583; 2001, Berlin, Springer.
71. C. B. Scruby and L. E. Drain: 'Laser ultrasonics: techniques and applications'; 1990, Bristol, A. Hilger.
72. O. N. Senkov, M. Dubois and J. J. Jonas: *Metall. Mater. Trans. A*, 1996, **A27**, 3963.
73. F. G. Wilson and T. Gladman: *Int. Mater. Rev.*, 1988, **33**, 221.
74. H. F. Poulsen, X. Fu, E. Knudsen, E. M. Lauridsen, L. Margulies and S. Schmidt: *Mater. Sci. Forum*, 2004, **467–470**, 1363.
75. H. F. Poulsen, E. M. Lauridsen, S. Schmidt, L. Margulies and J. H. Driver: *Acta Mater.*, 2003, **51**, 2517.
76. S. Mishra: 'Grain growth in the heat-affected zone of Ti-6Al-4V alloy welds: measurements and MC simulations', Masters dissertation, The Pennsylvania State University, PA, USA, 2003.
77. R. D. Doherty: *J. Mater. Educ.*, 1984, **6**, 841.
78. Z. Yang, S. Sista, J. W. Elmer and T. DebRoy: *Acta Mater.*, 2000, **48**, 4813.
79. S. Sista: 'Computer simulation of grain growth in three dimensions by Monte Carlo technique', Masters dissertation, The Pennsylvania State University, PA, USA, 2000.
80. J. S. Huang, J. Zhang, A. Cuevas and K. N. Tu: *Mater. Chem. Phys.*, 1997, **49**, 33.
81. R. E. Reed-Hill and R. Abbaschian: 'Physical metallurgy principles', 3rd edn, 256–264; 1992, Boston, PWS-KENT Publishing Company.
82. P. Feltham and G. J. Copley: *Acta Metall.*, 1958, **6**, 539.
83. F. J. Gil, J. A. Picas, J. M. Manero, A. Forn and J. A. Planell: *J. Alloy. Compd.*, 1997, **260**, 147.
84. A. K. Shah, S. D. Kulkarni, V. Gopinathan and R. Krishnan: *Weld. J.*, 1995, **74**, 325s.
85. J. C. Ion, K. E. Easterling and M. F. Ashby: *Acta Metall.*, 1984, **32**, 1949.
86. B. Radhakrishnan and T. Zacharia: *Metall. Mater. Trans. A*, 1995, **A26**, 2123.
87. S. L. Semiatin, V. Seetharaman, D. M. Dimiduk and K. H. G. Ashbee: *Metall. Mater. Trans. A*, 1998, **A29**, 7.
88. R. Kaspar and N. Mahmoud: *Mater. Sci. Technol.*, 1991, **7**, 249.
89. L. Zhang, C. B. Zhang, Y. M. Wang, S. Q. Wang and H. Q. Ye: *Acta Mater.*, 2003, **51**, 5519.
90. M. Kumar, R. Sasikumar and P. K. Nair: *Acta Mater.*, 1998, **46**, 6291.
91. M. Vandyoussefi and A. L. Greer: *Acta Mater.*, 2002, **50**, 1693.
92. T. Tsuta, T. Iwamoto and B. Wang: *Key Eng. Mater.*, 2003, **233–236**, 521.
93. T. Wang, J. Jin and X. Zheng: *J. Mater. Sci.*, 2002, **37**, 2645.
94. I. Loginova, G. Amberg and J. Agren: *Acta Mater.*, 2001, **49**, 573.
95. M. A. Fortes and A. Soares: in 'Modeling of coarsening and grain growth', (ed. S. P. Marsh and C. S. Pande), 257; 1993, Warrendale, PA, TMS.
96. B. E. S. Lindblom, L. Berthold and N. E. Hannerz: *Scand. J. Metall.*, 1991, **20**, 305.
97. P. Zhu and R. W. Smith: *Acta Metall. Mater.*, 1992, **40**, 683.
98. P. Zhu and R. W. Smith: *Acta Metall. Mater.*, 1992, **40**, 3369.
99. S. G. R. Brown, T. Williams and J. A. Spittle: *Acta Metall. Mater.*, 1994, **42**, 2893.
100. J. A. Spittle and S. G. R. Brown: *Acta Metall.*, 1989, **37**, 1803.
101. M. Rappaz, C.-A. Gandin, J. L. Desbiolles and P. Thevoz: *Metall. Mater. Trans. A*, 1996, **A27**, 695.
102. A. Jacot and M. Rappaz: *Acta Mater.*, 1997, **45**, 575.
103. V. V. Ploshikhin and H. W. Bergmann: in 'Mathematical modelling of weld phenomena 4', (ed. H. Cerjak), 150; 1998, London, IOM Communications.
104. A. Kermanpur, W. Wang, P. D. Lee and M. McLean: *Mater. Sci. Technol.*, 2003, **19**, 859.
105. J. Geiger, A. Roosz and P. Barkoczy: *Acta Mater.*, 2001, **49**, 623.
106. Y. Liu, T. Baudin and R. Penelle: *Scr. Mater.*, 1996, **34**, 1679.
107. D. J. Srolovitz, M. P. Anderson, G. S. Grest and P. S. Sahni: *Acta Metall.*, 1984, **32**, 1429.
108. G. Abbruzzese and K. Lucke: *Mater. Sci. Forum*, 1992, **94–96**, 597.
109. S. Sista, Z. Yang and T. DebRoy: *Metall. Mater. Trans. B*, 2000, **B31**, 529.
110. W. B. Hutchinson: *Int. Met. Rev.*, 1984, **29**, 25.
111. R. Sasikumar, E. Jacob and B. George: *Scr. Mater.*, 1998, **38**, 693.
112. W. Kurz, B. Giovanola and R. Trivedi: *Acta Metall.*, 1986, **34**, 823.
113. K. Goebbels: 'Materials characterization for process control and product conformity'; 1994, Boca Raton, Florida, CRC Press.
114. M. Militzer, R. Pandi and E. B. Hawbolt: *Metall. Mater. Trans. A*, 1996, **A27**, 1547.
115. C. Y. Wang and C. Beckermann: *Metall. Trans. A*, 1993, **A24**, 2787.
116. M. Rappaz: *Int. Mater. Rev.*, 1989, **34**, 93.
117. C. Y. Wang and C. Beckermann: *Metall. Mater. Trans. A*, 1994, **A25**, 1081.
118. L.-Q. Chen: *Annu. Rev. Mater. Res.*, 2002, **32**, 113.
119. D. Fan, C. Geng and L.-Q. Chen: *Acta Mater.*, 1997, **45**, 1115.
120. C. E. Krill and L.-Q. Chen: *Acta Mater.*, 2002, **50**, 3057.
121. J. P. Simmons, C. Shen and Y. Wang: *Scr. Mater.*, 2000, **43**, 935.
122. S. M. Allen and J. W. Cahn: *Acta Metall.*, 1979, **27**, 1085.
123. A. L. Wilson, R. P. Martukanitz and P. R. Howell: Proc. 5th Int. Conf. on 'Trends in welding research', (ed. J. M. Vitek *et al.*), 161; 1999, Materials Park, OH, ASM International.
124. Z. Yang, J. W. Elmer, J. Wong and T. DebRoy: *Weld. J.*, 2000, **79**, 97s.
125. J. Gao, R. G. Thompson and Y. Cao: Proc. 4th Int. Conf. on 'Trends in welding research', (ed. H. B. Smartt *et al.*), 199; 1996, Materials Park, OH, ASM International.
126. G. S. Grest, D. J. Srolovitz and M. P. Anderson: *Acta Metall.*, 1985, **33**, 509.
127. M. P. Anderson, G. S. Grest and D. J. Srolovitz: *Scr. Metall.*, 1985, **19**, 225.

128. Y. Saito: *ISIJ Int.*, 1998, **38**, 559.
129. E. Ising: *Z. Phys.*, 1925, **31**, 253.
130. J. A. Glazier, M. P. Anderson and G. S. Grest: *Philos. Mag. B*, 1989, **B62**, 1318.
131. Z. Yang: 'Modeling weldment macro and microstructure from fundamentals of transport phenomena and phase transformation theory', PhD thesis, The Pennsylvania State University, PA, USA, 2000.
132. S. Mishra and T. DebRoy: Proc. 6th Int. Conf. on 'Trends in welding research', (ed. S. A. David *et al.*), 197; 2003, Materials Park, OH, ASM International.
133. M.-Y. Li and E. Kannatey-Asibu, Jr: *Weld. J.*, 2002, **81**, 37s.
134. R. M. Miranda and M. A. Fortes: *Mater. Sci. Eng. A*, 1989, **A108**, 1.
135. W. Zhang, G. G. Roy, J. W. Elmer and T. DebRoy: *J. Appl. Phys.*, 2003, **93**, 3022.
136. W. Zhang, C.-H. Kim and T. DebRoy: *J. Appl. Phys.*, 2004, **95**, 5210.
137. X. He, P. Fuerschbach and T. DebRoy: *J. Appl. Phys.*, 2003, **94**, 6949.
138. A. Kumar and T. DebRoy: *J. Appl. Phys.*, 2003, **94**, 1267.
139. J. J. Pepe and W. F. Savage: *Weld. J.*, 1967, **46**, 411s.
140. W. W. Mullins: *J. Appl. Phys.*, 1956, **27**, 900.
141. D. A. Aboav and T. G. Langdon: *Metallography*, 1969, **1**, 333.
142. D. A. Aboav and T. G. Langdon: *Metallography*, 1969, **2**,171.
143. D. A. Aboav: *Metallography*, 1980, **13**, 43.
144. D. A. Aboav: *Metallography*, 1970, **3**, 383.
145. M. E. Glicksman, K. Rajan, J. Nordberg, M. Palmer, S. P. Marsh and C. S. Pande: *Mater. Sci. Forum*, 1992, **94–96**, 909.
146. S. B. Singh and H. K. D. H. Bhadeshia: *Mater. Sci. Technol.*, 1998, **14**, 832.
147. F. Wakai, N. Enomoto and H. Ogawa: *Acta Mater.*, 2000, **48**, 1297.